DYNAMICAL CHARACTERIZATION OF THERMOACOUSTIC OSCILLATIONS IN A HYDROGEN-ENRICHED PARTIALLY PREMIXED SWIRL-STABILIZED METHANE/AIR COMBUSTOR

Abhishek Kushwaha*, Praveen Kasthuri, Samadhan A. Pawar, R. I. Sujith

Department of Aerospace Engineering

Indian Institute of Technology Madras, Chennai - 600036, India

Ianko Chterev, Isaac Boxx

Institute for Combustion Technology

German Aerospace Centre (DLR), 70569 Stuttgart, Germany

ABSTRACT

In this study, we systematically analyze the effects of hydrogen enrichment in the well-known PRECCINSTA burner, a partially premixed swirl-stabilized methane/air combustor. Keeping the equivalence ratio and thermal power constant, we vary the hydrogen percentage in the fuel. Successive increments in hydrogen fuel fraction increase the adiabatic flame temperature and also shift the dominant frequencies of acoustic pressure fluctuations to higher values. Under hydrogen enrichment, we observe the emergence of periodicity in the combustor resulting from the interaction between acoustic modes. As a result of the interaction between these modes, the combustor exhibits a variety of dynamical states, including period-1 limit cycle oscillations (LCO), period-2 LCO, chaotic oscillations, and intermittency. The flame and flow behavior is found to be significantly different for each dynamical state. Analyzing the coupled behavior of the acoustic pressure and the heat release rate oscillations during the states of thermoacoustic instability, we report the occurrence of 2:1 frequency-locking during period-2 LCO, where two

*Corresponding author email: abhikushwaha8090@gmail.com

cycles of acoustic pressure lock with one cycle of the heat release rate. During period-1 LCO, we notice 1:1 frequency-locking, where both acoustic pressure and heat release rate repeat their behavior in every cycle.

NOMENCLATURE

TAI Thermoacoustic instability

LCO Limit cycle oscillations

HFF Hydrogen fuel fraction

ISL Inner shear layer

OSL Outer shear layer

IRZ Inner recirculation zone

ORZ Outer recirculation zone

ϕ Equivalence ratio

P Thermal power (kW)

p' Pressure fluctuations (kPa)

$\dot{q}'$ Global heat release rate fluctuations (a.u.)

P1 Period-1

P2 Period-2

I Intermittency

CO1 Chaotic state-1

CO2 Chaotic state-2

1 INTRODUCTION

The increasing trends in the deployment of renewable power generation (particularly solar and wind) are fuelling the need to develop novel technologies to overcome the mismatch between the available power and the ever-changing demand of the consumers [1]. Simultaneously, the advent of gas turbine combustors based on hydrogen blended fuels promises substantial reductions in greenhouse emissions [2]. In the current scenario, the integration of hydrogen with natural gas in the fuel used in power producing gas turbine engines is a promising green power alternative to achieve both emission and operational goals. Hence, the dynamics of hydrogen enriched combustion in modern swirl stabilized burners is of great interest to the community.

Generally, when power generating gas turbine engines running on unblended hydrocarbon fuels are operated on lean conditions, they are susceptible to thermoacoustic instability (TAI) characterized by large amplitude acoustic pressure and heat release rate oscillations.

This phenomenon can cause structural damage to the engines, resulting in unscheduled shutdowns and loss of revenue [1]. Hence, the effect of hydrogen enrichment on combustion stability is also of practical interest.

Right from the beginning of this century, hydrogen blended hydrocarbon fuels have been of interest to the gas turbine engine operators [3]. Hydrogen addition widens the lean flammability limits and allows the combustor to be operated at lower equivalence ratios. This ensures lower temperatures in the combustion zone, thereby reducing NO_x emissions [4]. Further, the reaction zone may shift to downstream locations in the combustor due to the higher flame speed and, the wider flammability allowed by hydrogen blended fuels [5 6]. Emadi *et al.* [7] reported that the hydrogen enrichment leads to increased burn rate and flame wrinkling due to enhanced interaction of small scale turbulence with the flame surface. Taamallah *et al*. [8] showed the existence of intermittent unstable acoustic pressure oscillations before the occurrence of fully developed TAI as they increased the equivalence ratio in the presence and absence of hydrogen. Palies *et al.* [9] showed a transition from stable to unstable operation via intermittent oscillations with an increase in equivalence ratio in a hydrogen-enriched premixed low swirl burner. Zhang *et al.* [10] investigated the dynamics of a hydrogen enriched methane/air combustor and identified three distinct states, which they call as stable, conditionally unstable, and unstable. They reported that hydrogen enrichment under high bulk flow velocities can excite TAI.

In this paper, we characterize the dynamical behavior of PRECCINSTA burner [11] for different conditions of hydrogen enrichment in methane at atmospheric pressure. The PRECCINSTA burner is a partially-premixed, swirl-stabilized combustor designed to capture much of the complexity of combustion in a gas turbine engine [12]. Over the past decade, several researchers have examined the combustion dynamics of the PRECCINSTA burner configuration both experimentally [11 13 14] and numerically [15–17] to understand the flame dynamics, vortex dynamics, fuel-air mixing, flame-acoustic coupling, etc. Recently, the investigation of the effect of hydrogen enrichment in fuel on the flame dynamics and the state of thermoacoustic instability is gaining increased attention in this system. Chterev *et al.* [18] investigated the impact of hydrogen addition in the PRECCINSTA burner operated with methane/air at atmospheric condition. They observed that the addition of hydrogen makes the flame compact and changes its shape from M to V configuration. Further, it increases the dominant frequencies of unstable acoustic modes and also affects the amplitude of thermoacoustic oscillations. Thus, hydrogen enrichment can strengthen or suppress thermoacoustic instability. Furthermore, they examined the effect of hydrogen enrichment in this system under elevated pressure conditions [14]. After hydrogen addition, they found that the amplitude of acoustic pressure oscillations during the occurrence of TAI is based on the phase delay between the Helmholtz acoustics and the heat release rate fluctuations in the combustor. Although some progress has been made recently on characterizing the dynamics of H_2-enriched PRECCINSTA burner, a full understanding of the different dynamical states resulting due to H_2 enrichment and the underlying mechanisms behind such combustion dynamics is still elusive.

In the present work, we apply different tools from dynamical systems theory [19] to analyze various dynamical states observed in a PRECCINSTA burner for different operating conditions during hydrogen enrichment. The application of dynamical systems theory and complex systems theory has recently introduced many tools to characterize the nonlinear behavior of thermoacoustic oscillations

[20 21]. Using dynamical systems approaches, several manifestations of thermoacoustic instability [22] such as limit cycle [23 24], quasiperiodicity [25], chaos [26–29], strange nonchaos [30], and intermittency [31–35] have been identified.

We found that the hydrogen enrichment of fuel leads to the interaction of unstable modes of the combustor. This, in turn, causes the occurrence of various dynamical states in the system such as period-1 LCO, period-2 LCO, intermittency and chaotic oscillations. We also study the flame and the flow dynamics during these states and characterize the coupling between the acoustic pressure and heat release rate fluctuations during different states of thermoacoustic oscillations.

2 EXPERIMENTAL SETUP

Measurements were performed at atmospheric pressure in the technically premixed gas turbine model combustor (PRECCINSTA configuration) shown in Fig. 1. In this combustor, air enters a cylindrical plenum and then passes through a swirl generator with 12 radial swirl channels. Fuel (methane with varying levels of hydrogen admixture) is injected through a 1 mm orifice in each swirl channel. The partially premixed swirling reactant flow then enters a combustion chamber through a conical nozzle with an exit diameter of 27.85 mm. The chamber has a square cross-section area of 85 × 85 mm^2 and a height of 114 mm. Optical access to the chamber is provided by the side walls made of quartz glass held by metal posts in the corners. The combustor exit consists of a conical contraction followed by an exhaust duct.

The pressure in the combustion chamber was measured using amplitude and phase calibrated microphone probe equipped with B&K Type 4939 condenser microphone located at a distance of 20 mm from the dump plane and sampled at a rate of 100 kHz.

Three components of velocity were measured in a plane aligned with the burner center-line using stereoscopic particle image velocimetry (PIV) technique. The stereo-PIV system consists of a dual-cavity, diode-pumped, solid state laser (Edgewave, IS200-2-LD, up to 9 mJ/pulse at 532 nm) and a pair of CMOS cameras (Phantom v1212) mounted on opposite sides of the laser sheet, looking down into the combustor. For each operating condition, 10,000 PIV image pairs were acquired over a 640 × 800 pixel resolution. The projected pixel resolution of the PIV system was 0.08 mm/pixel. The PIV measurement domain spans a region of 65 × 50 mm^2, (-32 $< x <$ 32 mm and 0 $< y <$ 50 mm in Fig. 1). The inter-frame pulse separation (Δt) was set to 10 ms. The beam was formed into a sheet using a pair of cylindrical lenses (f = -38 mm and 250 mm) and thinned to a waist using a third cylindrical lens (f = 700 mm). The combustion air flows were seeded with titanium dioxide particles of a nominal diameter of 1 μm. Image mapping, calibration, and particle cross-correlations were completed using a commercial, multi-pass adaptive window offset cross-correlation algorithm (LaVision DaVis 10). Final interrogation window size and overlap were 16 × 16 pixels and 50%, respectively, corresponding to a window size of 1.3 mm and vector spacing of 0.65 mm. The uncertainty in the instantaneous velocities based on the correlation statistics in DaVis was estimated to be $\approx$ 0.7 m/s for the in-plane components ($x-y$) and $\approx$ 1.8 m/s for the out-of-plane component (z-axis).

The line of sight integrated chemiluminescence from the self-excited OH* radical was imaged over a 512 x 512 pixel resolution with an intensified high-speed CMOS camera (LaVision HSS 5 with LaVision HS-IRO) equipped with a fast UV objective lens (Halle, f

= 64 mm, f/2.0) and a bandpass filter (300–325 nm). The intensifier gate time was between 25 and 50 μs depending on signal strength. The onboard memory of the camera enabled the acquisition of 8192 frames per recording. The intensity from all the pixels is integrated to obtain the global heat release rate $\dot{q}'$ signal.

The OH - planar laser-induced fluorescence (PLIF) imaging system is based on a frequency-doubled dye laser, pumped by high-speed, pulsed Nd:YAG laser (Edgewave IS400-2-L, 150 W at 532 nm and 10 kHz) and an intensified high-speed CMOS camera system. The dye laser system (Sirah Credo) produced 5.3 to 5.5 W at 283 nm and 10 kHz repetition rate (i.e. 0.53-0.55 mJ/pulse). The dye laser was tuned to excite the $Q_1(6)$ line of the $A^2\sum^+ - X^2\prod (v'=1, v''=0)$ band. The laser wavelength was monitored continuously throughout the experiments using a photo-multiplier tube (PMT) fitted with WG-305 and UG-11 filters and a premixed, laminar reference flame. The 283-nm PLIF excitation beam is formed into a sheet approximately 50 mm (high) × 0.2 mm (thick) using three fused-silica, cylindrical lenses (all *anti-reflective* coated to maximize transmission).

OH-PLIF fluorescence signal was imaged using a high-speed CMOS camera (LaVision HSS6) and external two-stage intensifier (LaVision HS-IRO) mounted on the opposite side of the combustor with respect to the OH camera. The OH-PLIF camera was equipped with another fast UV objective lens (Cerco, f = 45 mm, f/1.8) and a bandpass filter (300–325 nm). The projected pixel resolution of the camera was 0.115 mm/pixel, with an array size of 768 × 768 pixels. The OH-PLIF images covered a measurement domain that extended over the entire width ($-42.5 < x < 42.5$ mm), and was illuminated to an axial distance of $0 < y < 50$ mm. The OH*-chemiluminescence, OH-PLIF and stereo-PIV images were acquired at a rate of 10 kHz simultaneous with the microphone measurements.

Data were collected at three thermal load conditions, P = 10, 15 and 20 kW. and two equivalence ratios, ϕ = 0.65 and 0.8 (see Table 1). The equivalence ratio and thermal power are maintained constant by appropriate mass balancing amongst the reactants. For each combination of thermal load and equivalence ratio, the fraction of hydrogen in the fuel was varied from 0 – 80%, in increments of 10%. This gives a parameter space of 54 operational test conditions, albeit with some cases invoking strong thermoacoustic pulsations which shattered the windows of the combustion chamber, rendering the conditions unviable for measurement. The hydrogen fuel fraction (HFF) can be defined as, $HFF = \dot{V}_{H_2}/(\dot{V}_{H_2} + \dot{V}_{CH_4})$. Here, $\dot{V}$ represents the standard volume flow rate in hydrogen or methane. Hereon, low/high HFF implies that the volume flow rate of hydrogen is less/more than that of methane.

3 RESULTS AND DISCUSSION

First, we briefly present the effect of hydrogen addition in the combustor for two equivalence ratios and three thermal powers before performing a detailed characterization of each dynamical state observed in the system. We observe that the addition of hydrogen in the fuel alters the combustion dynamics significantly. This is reflected in the occurrence of several rich dynamical states in the acoustic pressure fluctuations (p') of the combustor. In Table.1, we show the different dynamical states observed in the p' signal due to an increase in HFF in the fuel under different operating conditions. The characteristics of these states are elaborated in Sec. 3.1. We notice the following overall changes in the system behavior.

When the system is operated at low thermal power (P = 10 kW) for both ϕ = 0.65 and 0.8, we observe emergence of periodic oscillations due H_2 enrichment. We notice the presence of low amplitude chaotic state-1 oscillations (CO1), low amplitude P1 LCO, and intermittency for increasing HFF. As the thermal power is increased to a higher value (P = 15 kW), for values of ϕ = 0.65 and 0.8 at 0% HFF, we observe the simultaneous excitation of two modes (f_1 and f_2) in the system. As these modes are rationally related to each other in a ratio of f_1/f_2 = 2, we refer to them as period-2 (P2) LCO. For $\phi = 0.65$, we notice that the system stays in the state of P2 LCO for lower HFF; however, it exhibits chaotic state-2 (CO2) oscillations for higher HFF. In contrast, at a higher value of ϕ = 0.8, the system shows P2 LCO for lower HFF, that transition to P1 LCO via chaotic oscillations (CO2) as HFF is increased. We observe only CO2 oscillations at higher HFF. At the higher thermal power (P = 20 kW) and $\phi = 0.65$, the system exhibits low amplitude chaotic oscillations (CO1) for lower HFF, while P2 LCO and P1 LCO are noticed at higher HFF. For ϕ = 0.8, we notice CO2 oscillations in the pressure dynamics at all hydrogen enrichment levels.

Thus, the overall comparison of the results for different operating conditions suggests that, the addition of H_2 to the fuel at different operating conditions, generates or suppresses the thermoacoustic instabilities (P1 or P2 LCOs), or leads to the complex dynamics resulting from the interaction of modes that are integer multiples of each other (chaotic oscillations) in the combustor.

Next, we perform a detailed characterization of the temporal dynamics and the flow/flame dynamics corresponding to key dynamical states observed in the system due to hydrogen enrichment in the fuel.

3.1 Dynamical states due to hydrogen enrichment

3.1.1 Period-1 limit cycle oscillations Figure. 2a represents the p' signal observed when the system operates at the condition of TAI. During this dynamical state, we observe the presence of large amplitude periodic oscillations. The power spectrum of this signal (Fig. 2d) shows a dominant peak at 415 Hz and a small magnitude peak at its harmonic observed at 830 Hz. The presence of oscillations having a single dominant frequency is further confirmed by the corresponding scalogram (Fig. 2b), which shows the presence of a nearly constant magnitude for 415 Hz throughout the signal. The reconstructed phase space of this state shows a ring-like structure (Fig. 2c), typically observed for P1 LCO [22]. For some conditions, we observe a weakly P1 LCO which are significantly influenced by the turbulent fluctuations. We briefly describe their characteristics in Supplementary material S4.

The normalized p' and $\dot{q}'$ signals show a phase difference of around 28°, indicating the presence of in-phase synchronous oscillations during the state of P1 LCO (Fig. 3I). This behavior is in accordance with the Rayleigh criterion [36]. During this state, we observe large sized vortices shed periodically along the ISL in the flow field (Fig. 3II). We observe significant intensity variations in the flame stabilized in the region between the ISL and OSL along the two branches (Fig. 3III), as the pressure amplitude varies between its maxima to minima. When the pressure amplitude is near its maxima (Fig. 3Ia), we observe nearly a symmetric generation of vortices in ISLs from the dump plane (Figs. 3IIa,e) and a very high flame intensity in the flow field (Figs. 3IVa,b). The flame is wider and appears asymmetric across all time instants (Fig. 3III). As the pressure goes from minima to maxima (Figs. 3Ic-e), we notice a pronounced wrinkling along the flame

(see Fig. 3IIId) as the vortices convect downstream. Simultaneously, we also notice an increase in the flame intensity from its minima to maxima (Figs. 3IVc-e). This flame behavior is observed to repeat for every cycle.

3.1.2 Period-2 limit cycle oscillations Apart from the most widely studied P1 LCO characterized by a single timescale in swirl combustors [37 38], we also observe the presence of limit cycle oscillations characterized by two dominant timescales (Fig. 4) in our system. We refer to such oscillations as period-2 limit cycle oscillations. During this state, we notice the repetition of the signal behavior for every two cycles of oscillations. The power spectrum of this state illustrates two frequencies ($f_1 = 283$ Hz, $f_2 = 568$ Hz, and $f_2/f_1 \approx 2$) of comparable amplitudes (Fig. 4d). From the scalogram plot (Fig. 4b), we observe that these two frequencies are continuously present in the signal. However, the amplitude at $f_2 = 568$ Hz is time varying, while $f_1 = 283$ Hz exhibits a near constant amplitude throughout the signal in the scalogram (Fig. 4b). Such behavior could lead to variable amplitude loading in the combustor [39]. In the corresponding phase space of this state (Fig. 4c), we observe that the phase space trajectory performs a smaller inner loop for every revolution around the bigger outer loop, typical of P2 LCO [22].

We notice significant changes in the flow and the flame dynamics during this state as compared to that observed during the P1 LCO state. When the pressure amplitude is at point *a* (Fig. 5I), we notice the flame is stretched, and most of the heat release rate happens far downstream of the dump plane of the combustor (Fig. 5IVa). The distribution of OH-field is observed to be very high near the inlet in the IRZ of the flame (Fig. 5IIIa). As the pressure approaches the first local minima (point b in Fig. 5I), the heat release rate is low in the combustor (Fig. 5IVb). The corresponding distribution of OH-field appears to be nearly uniform in the central plane (Fig. 5IIIb). As the pressure reaches the second local maxima and the second local minima (points c and d in Fig. 5I), the flame exhibits a thin jet-like structure (Figs. 5IVc,d), while we see low concentration of OH-field scattered over small regions (Figs. 5IIIc,d). The PIV images of the flow field show that when the pressure is at the first local minima (Fig. 5IIb), a vortex is shed along the OSL from the dump plane. This vortex then grows to its maximum size as the pressure reaches the second local minima (Fig. 5IId). After this instant, this vortex breaks down and causes an increase in the local heat release rate in the system, coinciding with the pressure maxima (Fig. 5IIe). This behavior of the flame repeats for every two oscillation cycles in the system.

3.1.3 Intermittency In Fig. 6, we show the state of intermittency observed in the combustor. The state of intermittency [32] is characterized by the occurrence of epochs of low amplitude aperiodic oscillations amidst bursts of large-amplitude periodic oscillations interspersed in an apparently random manner (Fig. 6a). Such oscillations have been reported in many turbulent thermoacoustic systems previously [34354041]. The scalogram (Fig. 6b) corresponding to this state shows the intermittent occurrence of the dominant frequency at $f = 351$ Hz in the signal. In the accompanying power spectrum (Fig. 6d), we notice the presence of broadband frequencies having a peak around 351 Hz. Figure 8c shows the reconstructed phase portrait during the state of intermittency. We observe a clutter of trajectories at the centre of the phase portrait due to aperiodic oscillations. These trajectories then spiral towards the distant regular

ring-like attractor during the occurrence of bursts of periodicity in the signal, before being re-injected back to the center of the ring at the end of the burst. The flow and flame dynamics corresponding to this state need to be studied separately during aperiodic and periodic epochs. We qualitatively describe the flame and flow behavior during intermittency in Supplementary material (refer to Figs. S2, S3).

3.1.4 Chaotic oscillations We observe two kinds of chaotic oscillations in the combustor. We refer to these two states as chaotic state-1 (CO1) and chaotic state-2 (CO2), respectively. The reasons behind making the distinction between the two chaotic states will become apparent after their descriptions.

In Figs. 7a,b, we show the p' signal and the scalogram corresponding to chaotic state-1 oscillations (CO1). The amplitude as well as the frequency of these oscillations shows a significant variation in time. The corresponding power spectrum shows several broadband frequencies without any distinguishable peak (Fig. 7d). In the reconstructed phase space (Fig. 7c) of this state, we observe the phase space trajectory spiralling inwards and outwards in a haphazard manner.

In Figs. 8a,b, we show the p' signal and the scalogram corresponding to chaotic state-2 oscillations (CO2). The amplitude during CO2 is appreciably higher than that recorded during CO1. Furthermore, the frequency does not vary considerably in time. As a result, from the corresponding power spectrum (Fig. 8d), we see distinct frequency peaks. However, the reconstructed phase space (Fig. 8c) of this state is similar to that observed in CO1. Finally, the flame and flow behaviors during both CO1 and CO2 are considerably different to each other and are described in Supplementary material S2 (Figs. S4 and S5).

In order to qualitatively confirm the presence of chaos, we performed the 0-1 test [42]. Let us consider the input time series to be $\gamma(t)$. The first step is to compute the translation variables $x(n)$ and $y(n)$ such that

$$\begin{aligned} x(n) &= \sum_{j=1}^{n} \gamma(t)\ cos\ (tc) \\ y(n) &= \sum_{j=1}^{n} \gamma(t)\ sin\ (tc). \end{aligned} \tag{1}$$

Here, n = 1,2,...,N, where N is the total number of data points in time series. For our analysis, we have selected the value of c in the interval $(\pi/5, 4\pi/5)$ [28]. The behavior of these two translation variables helps in determining the existence of chaos in the system. For periodic or quasiperiodic oscillations, these variables show bounded behavior. However, for chaotic dynamics, their behavior is unbounded and irregular. The behavior of the trajectory in the $x(n) - y(n)$ plane for increasing n can be computed with the help of modified mean square displacement $M(n)$ as follows:

$$M(n) = \frac{1}{N}\sum_{J=1}^{n}[\,(x(j+n)-x(j))^2+(y(j+n)-y(j))^2]-\frac{1}{N}\sum_{j=1}^{n}\gamma(t)\frac{1-cos\,(jc)}{1-cos\,(c)}) \tag{2}$$

For a chaotic state, $M(n)$ exhibits a monotonic increasing trend with n, while it becomes nearly constant for regular states. The asymptotic growth of the mean displacement is computed with the help of linear regression, as follows:

$$K = \lim_{n\to\infty}\frac{\log M(n)}{\log n}. \tag{3}$$

The value of K lies between 0 and 1. For a chaotic signal, K takes a value close to 1, and for a regular signal, it approaches a value close to 0 [42]. We need to use the pressure data at an optimal sampling rate for performing this test [43]. The methodology followed to obtain the optimally undersampled signal is discussed in Supplementary material S3.

In Fig. 9, we show the results obtained from the 0-1 test for the optimally undersampled pressure signal obtained during CO1 and CO2 states. The trajectories in the $x(n)-y(n)$ plane (Figs. 9a(i),b(i)) show a near random behavior for both the states. The variation of $M(n)$ with n exhibits an increasing trend (Figs. 9a(ii),b(ii)). Further, the value of K shows fluctuations near 1 (Figs. 9a(iii),b(iii)). The median value of K is observed to be 0.99 and 0.98 for CO1 and CO2, respectively.

We also confirmed the presence of chaos with the help of recently developed *Chaos Decision Tree algorithm* by Toker *et al.* [44]. Following this algorithm, we obtained $K = 0.99$ and 0.93 for CO1 and CO2 states, respectively. Therefore, the results from the 0-1 test as well as the *Chaos Decision Tree algorithm* substantiates the existence of chaos in the combustor. The description of the *Chaos Decision Tree algorithm* is provided in the Supplementary material S3.

3.2 Transition from period-2 to period-1 oscillations due to mode interaction with H_2 enrichment

In this section, we discuss the dynamical transition in the system as HFF is increased from 0% to 60% while maintaining the same equivalence ratio and thermal power. Figure 10 represents the effect of increase in HFF for the operating conditions of P = 15 kW and ϕ = 0.8 mentioned in Table 1. For HFF = 0%, p' show the characteristics of P2 oscillations (Fig. 10Ia). We also plot the amplitude spectrum (Fig. 10IIb) which exhibits the presence of two peaks (f_1 = 260 Hz and f_2 = 520 Hz) with comparable amplitude (P(f_1)/P(f_2) < 5). Accordingly, the phase space trajectory is bounded by a double-looped attractor (Fig. 10IIIa) and the first return map contains two clusters (Fig. 10IVa). Here, the return map [19] is obtained by plotting the successive local maximas of a p' signal in time. A small

addition of HFF leads to a reduction in the amplitude of P2 oscillations (Fig. 10Ib). On further increase in HFF beyond 10%, we observe a significant decrease in the amplitude of frequencies at both modes of the p' signal (Figs. 10IIc to 10IIe). As a consequence, we notice a change in the system dynamics from P2 LCO to chaotic state-2. The amplitude spectrum (Figs. 10IIc to 10IIe) shows the shift in both peaks to a higher value. The phase space trajectories of this state show a cluttered behavior due to the interaction of multiple broadband frequencies (Figs. 10IIIc to 10IIIe). The first return map shows a cluster of points along the diagonal line (Figs. 10IVc to 10IVe).

For HFF = 50%, we notice the occurrence of a considerably high amplitude P1 LCO in the system (Fig. 10If). The corresponding amplitude spectrum (Fig. 10IIf) displays a dominant frequency at (f = 586 Hz) with very high amplitude. The phase space (Fig. 10IIIf) of this state exhibits a ring-like attractor. The first return map for this case shows a cluster of points on the diagonal for larger amplitudes (Fig. 10IVf). Similar behavior is also observed for HFF = 60% (Fig. 10Ig). Therefore, we observe the change of the system behavior from P2 to P1 oscillations via chaotic oscillations as HFF is increased.

We also notice a gradual increase in the frequencies of the fundamental and harmonic modes due to the increasing content of H_2 in the fuel (see Fig. 10III). This increase in the unstable frequencies of the system happens due to an increase in the adiabatic temperature of the flame (refer to Supplementary material S1). The adiabatic flame temperature increases by about 100 K as HFF is increased from 0% to 80%. Thus, hydrogen enrichment of methane results in the occurrence of different dynamical states in the system, which can be attributed to the progressive shifting of the frequency and the interaction of unstable acoustic modes of the combustor.

3.3 Locking behavior of p' and $\dot{q}'$ oscillations during the states of thermoacoustic instability

As we know, a positive feedback (or mutual synchronization) between p' and $\dot{q}'$ fluctuations is mostly responsible for the occurrence of TAI [36]. Here, we analyze the coupled interaction between these fluctuations during the distinct states of TAI, i.e., P1 and P2 LCOs.

Towards this purpose, we plot the overlapped time series of p' and $\dot{q}'$ signals, normalized by their respective maximum values, corresponding to the state of P1 LCO in Fig. 11a. During this state, we observe that both p' and $\dot{q}'$ signals are in-phase synchronized, where every oscillation cycle of p' appears to be locked with that of $\dot{q}'$; thus, satisfying the Rayleigh's criterion [36]. In Figs. 11g,h, we represent spikes of unit magnitude corresponding to the time instants at which the corresponding p' and $\dot{q}'$ signals (Fig. 11f) attain the local maxima, respectively. We observe single local peak from both the signals in each cycle (indicated by dashed boxes $C_1, C_2, ...C_{18}$ in Figs. 11g,h). This is further confirmation of the fact that the p' and $\dot{q}'$ signals have the same frequency (Figs. 11g,h). Thus, during the state of P1 LCO, both p' and $\dot{q}'$ signals exhibit 1:1 frequency locking (mutual synchronization). The corresponding phase spaces for p' and $\dot{q}'$ (Figs. 11b,c) contain a single ring-like attractor, indicative of LCO . The first return maps for p' and $\dot{q}'$ (Figs. 12d,e) exhibit a single cluster of points at the diagonal line with high amplitudes.

Furthermore, we show the coupled dynamics of p' and $\dot{q}'$ signals observed during the state of P2 LCO in Fig. 12. The magnified views (Fig. 12f) of these signals show markers corresponding to their local maxima, which are captured by the spiking signals in

Figs. 12g,h. From Figs. 12g,h, we understand that in one cycle (denoted by $C_1, C_2, ..., C_{13}$ in Figs. 12g,h), there are two peaks in the p' signal and one peak in the $\dot{q}'$ signal (see blue dashed rectangle in Figs. 12g,h). This means that p' signal exhibits two oscillations in a single period, while $\dot{q}'$ signal exhibits a single oscillation in the same period. This further indicates the presence of 2:1 frequency locking between p' and $\dot{q}'$ during the state of P2 LCO in the system. Note that both p' and $\dot{q}'$ signals have the same dominant frequency. The reconstructed phase spaces (Figs. 12b,c) and the first return maps (Figs. 12d,e) for p' and $\dot{q}'$, also confirms this locking behavior of the signals. For p' signal, the phase space has a two looped structure (Fig. 12b); in contrast, for the $\dot{q}'$ signal, the phase space contains a single ring-like structure (Fig. 12c). For p' signal, the first return map exhibits two prominent clusters at off-diagonal locations corresponding to two loops of the phase space trajectory and a small scatter of points along the diagonal line due to the underlying turbulent fluctuations. In contrast, we notice a single cluster of points in the return map of $\dot{q}'$ signal. Thus, we report the first observation of 2:1 frequency locking between mutually coupled p' and $\dot{q}'$ oscillations in a thermoacoustic acoustic system. We show the occurrence of 1:1 and 2:1 synchronization between the p' and $\dot{q}'$ signals during the state of TAI in the same combustor due to a change in the hydrogen enrichment level in the fuel.

4 CONCLUSIONS

We studied the effect of hydrogen enrichment in the dynamics of a technically premixed swirl-stabilized combustor under different conditions of thermal powers and equivalence ratios. We characterized different dynamical states ranging from period-1 LCO, period-2 LCO, intermittency, and chaotic oscillations observed in the system. We distinguished two chaotic states occurring in the combustor based on their dynamical behavior. For varying levels of hydrogen enrichment, these dynamical states occur due to the combined effects of increasing dominant frequencies and the interaction amongst unstable acoustic modes of the combustor. We also studied the transition of period-2 LCO to period-1 LCO via chaotic oscillations characterized by interactions between various acoustic modes.

Furthermore, we observe that the flow and flame dynamics varies significantly depending on the dynamical state present in the combustor. When the combustor exhibits P1 LCO, the flame intensity changes periodically in between the inner and outer shear layers. However, during P2 LCO, the flame is stabilized mostly in the IRZ, and the flame shape is observed to be very thin at the base. Compared to P1 LCO, we found that the location of maximum heat release rate shifts farther away from the combustor inlet during P2 LCO.

We also show the existence of 2:1 frequency locking between the acoustic pressure and heat release rate oscillations during the state of period-2 LCO. This is different from the 1:1 frequency locking observed during the state of period-1 LCO. The occurrence of P1 and P2 limit cycle oscillations, would impose different amplitude loading on the combustor walls, which might demand additional structural reinforcements to the combustor.

5 ACKNOWLEDGEMENTS

This project has received funding from the European Research Council (ERC) under the European Union's Horizon 2020 research and innovation programme (Grant agreement No. 682383). R. I. Sujith is grateful to Science and Engineering Research Board, Department of Science and Technology, Government of India for providing financial support under grant number of JCB/2018/000034/SSC.

6 SUPPLEMENTARY MATERIAL

In S1, we have shown the variation of adiabatic flame temperature for increasing HFF using the GASEQ software, shown in Table. 1. In S2, we have discussed the flame and flow dynamics for the states of intermittency, chaotic state-1 and chaotic state-2. In S3, we have described the *Chaos Decision Tree algorithm* and methodology behind obtaining optimally sampled signal for 0-1 test. In S4, we discuss the characteristics of weakly periodic limit cycle oscillations.

REFERENCES

[1] Lieuwen, T. C., and Yang, V., 2005. *Combustion instabilities in gas turbine engines: operational experience, fundamental mechanisms, and modeling*. American Institute of Aeronautics and Astronautics.

[2] Schefer, R. W., Wicksall, D., and Agrawal, A., 2002. "Combustion of hydrogen-enriched methane in a lean premixed swirl-stabilized burner". *Proceedings of the combustion institute,* ***29***(1), pp. 843–851. DOI:10.1016/S1540-7489(02)80108-0.

[3] Beita, J., Talibi, M., Sadasivuni, S., and Balachandran, R., 2021. "Thermoacoustic instability considerations for high hydrogen combustion in lean premixed gas turbine combustors: A review". *Hydrogen,* ***2***(1), pp. 33–57. DOI:https://doi.org/10.3390/hydrogen2010003.

[4] Schefer, R., 2003. "Hydrogen enrichment for improved lean flame stability". *International Journal of Hydrogen Energy,* ***28***(10), pp. 1131–1141. DOI: 10.1016/S0360-3199(02)00199-4.

[5] Jackson, G. S., Sai, R., Plaia, J. M., Boggs, C. M., and Kiger, K. T., 2003. "Influence of h2 on the response of lean premixed ch4 flames to high strained flows". *Combustion and Flame,* ***132***(3), pp. 503–511. DOI: 10.1016/S0010-2180(02)00496-0.

[6] Kim, H. S., Arghode, V. K., Linck, M. B., and Gupta, A. K., 2009. "Hydrogen addition effects in a confined swirl-stabilized methane-air flame". *International journal of hydrogen energy,* ***34***(2), pp. 1054–1062. DOI: 10.1016/j.ijhydene.2008.10.034.

[7] Emadi, M., Karkow, D., Salameh, T., Gohil, A., and Ratner, A., 2012. "Flame structure changes resulting from hydrogen-enrichment and pressurization for low-swirl premixed methane–air flames". *International Journal of Hydrogen Energy,* ***37***(13), pp. 10397–10404. DOI: 10.1016/j.ijhydene.2012.04.017.

[8] Taamallah, S., LaBry, Z. A., Shanbhogue, S. J., and Ghoniem, A. F., 2015. "Thermo-acoustic instabilities in lean premixed swirl-stabilized combustion and their link to acoustically coupled and decoupled flame macrostructures". *Proceedings of the Combustion Institute,* ***35***(3), pp. 3273–3282. DOI:10.1016/j.proci.2014.07.002.

[9] Palies, P., Ilak, M., and Cheng, R., 2017. "Transient and limit cycle combustion dynamics analysis of turbulent premixed swirling flames". *Journal of Fluid Mechanics,* ***830***, pp. 681–707. DOI:10.1017/jfm.2017.575.

[10] Zhang, J., and Ratner, A., 2019. "Experimental study on the excitation of thermoacoustic instability of hydrogen-methane/air premixed flames under atmospheric and elevated pressure conditions". *International Journal of Hydrogen Energy,* ***44***(39), pp. 21324–21335. DOI:10.1016/j.ijhydene.2019.06.142.

[11] Meier, W., Weigand, P., Duan, X., and Giezendanner-Thoben, R., 2007. "Detailed characterization of the dynamics of thermoacoustic pulsations in a lean premixed swirl flame". *Combustion and Flame,* ***150***(1-2), pp. 2–26. DOI:10.1016/j.combustflame.2007.04.002.

[12] Lartigue, G., Meier, U., and Berat, C., 2004. "Experimental and numerical investigation of self-excited combustion oscillations in a scaled gas turbine combustor". *Applied thermal engineering,* ***24***(11-12), pp. 1583–1592. DOI:https://doi.org/10.1016/j.applthermaleng.2003.10.026.

[13] Oberleithner, K., Stöhr, M., Im, S. H., Arndt, C. M., and Steinberg, A. M., 2015. "Formation and flame-induced suppression of the precessing vortex core in a swirl combustor: experiments and linear stability analysis". *Combustion and Flame,* ***162***(8), pp. 3100–3114. DOI:10.1016/j.combustflame.2015.02.015.

[14] Chterev, I., and Boxx, I., 2020. "Effect of hydrogen enrichment on the dynamics of a lean technically premixed elevated pressure flame". *Combustion and Flame,* ***225***, pp. 149–159. DOI:10.1016/j.combustflame.2020.10.033.

[15] Bénard, P., Lartigue, G., Moureau, V., and Mercier, R., 2019. "Large-eddy simulation of the lean-premixed preccinsta burner with wall heat loss". *Proceedings of the Combustion Institute,* ***37***(4), pp. 5233–5243. DOI:https://doi.org/10.1016/j.proci.2018.07.026.

[16] Franzelli, B., Riber, E., Gicquel, L. Y., and Poinsot, T., 2012. "Large eddy simulation of combustion instabilities in a lean partially premixed swirled flame". *Combustion and flame,* ***159***(2), pp. 621–637. DOI:https://doi.org/10.1016/j.combustflame.2011.08.004.

[17] Wang, P., Platova, N., Fröhlich, J., and Maas, U., 2014. "Large eddy simulation of the preccinsta burner". *International Journal of Heat and Mass Transfer,* ***70***, pp. 486–495. DOI:https://doi.org/10.1016/j.ijheatmasstransfer.2013.11.025.

[18] Chterev, I., and Boxx, I., 2019. "Flame topology and combustion instability limits of lean premixed hydrogen enriched flames". In 27th International Colloquium on the Dynamics of Explosions and Reactive Systems, July 28 - August 2, Beijing, China. DOI:https://elib.dlr.de/130096/.

[19] Nayfeh, A. H., and Balachandran, B., 2008. *Applied nonlinear dynamics: analytical, computational, and experimental methods*. John Wiley & Sons.

[20] Sujith, R., and Unni, V. R., 2020. "Dynamical systems and complex systems theory to study unsteady combustion". *Proceedings of the Combustion Institute*. DOI: 10.1016/j.proci.2020.07.081.

[21] Juniper, M. P., and Sujith, R. I., 2018. "Sensitivity and nonlinearity of thermoacoustic oscillations". *Annual Review of Fluid Mechanics,* ***50***, pp. 661–689. DOI:https://doi.org/10.1146/annurev-fluid-122316-045125.

[22] Kabiraj, L., Saurabh, A., Wahi, P., and Sujith, R. I., 2012. "Route to chaos for combustion instability in ducted laminar premixed flames". *Chaos: An Interdisciplinary Journal of Nonlinear Science,* ***22***(2), p. 023129. DOI:10.1063/1.4718725.

[23] Culick, F., 1994. "Some recent results for nonlinear acoustics in combustion chambers". *AIAA journal,* ***32***(1), pp. 146–169. DOI: 10.2514/3.11962.

[24] Lieuwen, T. C., 2002. "Experimental investigation of limit-cycle oscillations in an unstable gas turbine combustor". *Journal of Propulsion and Power,* ***18***(1), pp. 61–67. DOI:https://doi.org/10.2514/2.5898.

[25] Sterling, J. D., 1993. "Nonlinear analysis and modelling of combustion instabilities in a laboratory combustor". *Combustion Science and Technology,* ***89***(1-4), pp. 167–179. DOI: 10.1080/00102209308924107.

[26] Keanini, R., Yu, K., and Daily, J., 1989. "Evidence of a strange attractor in ramjet combustion". In 27th Aerospace Sciences Meeting, p. 624. DOI: 10.2514/6.1989-624.

[27] Kabiraj, L., Saurabh, A., Karimi, N., Sailor, A., Mastorakos, E., Dowling, A. P., and Paschereit, C. O., 2015. "Chaos in an imperfectly premixed model combustor". *Chaos: An Interdisciplinary Journal of Nonlinear Science,* ***25***(2), p. 023101. DOI:https://doi.org/10.1063/1.4906943.

[28] Nair, V., Thampi, G., Karuppusamy, S., Gopalan, S., and Sujith, R., 2013. "Loss of chaos in combustion noise as a precursor of impending combustion instability". *International journal of spray and combustion dynamics,* ***5***(4), pp. 273–290. DOI:https://doi.org/10.1260/1756-8277.5.4.273.

[29] Gotoda, H., Nikimoto, H., Miyano, T., and Tachibana, S., 2011. "Dynamic properties of combustion instability in a lean premixed gas-turbine combustor". *Chaos: An Interdisciplinary Journal of Nonlinear Science,* ***21***(1), p. 013124. DOI:https://doi.org/10.1063/1.3563577.

[30] Premraj, D., Pawar, S. A., Kabiraj, L., and Sujith, R., 2020. "Strange nonchaos in self-excited singing flames". *EPL (Europhysics Letters),* ***128***(5), p. 54005. DOI: https://doi.org/10.1209/0295-5075/128/54005.

[31] Kabiraj, L., and Sujith, R., 2012. "Nonlinear self-excited thermoacoustic oscillations: intermittency and flame blowout". *Journal of Fluid Mechanics,* ***713***(376-397), p. 13. DOI:https://doi.org/10.1017/jfm.2012.463.

[32] Nair, V., Thampi, G., and Sujith, R. I., 2014. "Intermittency route to thermoacoustic instability in turbulent combustors". *Journal of Fluid Mechanics,* ***756***, pp. 470–487. DOI:10.1017/jfm.2014.468.

[33] Kheirkhah, S., Cirtwill, J. M., Saini, P., Venkatesan, K., and Steinberg, A. M., 2017. "Dynamics and mechanisms of pressure, heat release rate, and fuel spray coupling during intermittent thermoacoustic oscillations in a model aeronautical combustor at elevated pressure". *Combustion and Flame,* ***185***, pp. 319–334. DOI:https://doi.org/10.1016/j.combustflame.2017.07.017.

[34] Pawar, S. A., and Sujith, R. I., 2018. "Transition to thermoacoustic instability in a turbulent combustor". *Journal of the Combustion Society of Japan,* ***60***(192), pp. 99–111. DOI: 10.20619/jcombsj.60.192.99.

[35] Dutta, A. K., Ramachandran, G., and Chaudhuri, S., 2019. "Investigating thermoacoustic instability mitigation dynamics with a

kuramoto model for flamelet oscillators". *Physical Review E,* ***99***(3), p. 032215. DOI:https://doi.org/10.1103/PhysRevE.99.032215.

[36] Rayleigh, J. W. S., 1878. "The explanation of certain acoustical phenomena". *Nature,* ***18***(455), pp. 319–321. DOI:10.1038/018319a0.

[37] Gotoda, H., Shinoda, Y., Kobayashi, M., Okuno, Y., and Tachibana, S., 2014. "Detection and control of combustion instability based on the concept of dynamical system theory". *Physical Review E,* ***89***(2), p. 022910. DOI: 10.1103/PhysRevE.89.022910.

[38] Pawar, S. A., Mondal, S., George, N. B., and Sujith, R. I., 2018. "Synchronization behaviour during the dynamical transition in swirl-stabilized combustor: temporal and spatiotemporal analysis". In 2018 AIAA Aerospace Sciences Meeting, p. 0394. DOI: 10.2514/6.2018-0394.

[39] Suresh, S., 1998. *Fatigue of materials*. Cambridge university press.

[40] Sampath, R., and Chakravarthy, S. R., 2016. "Investigation of intermittent oscillations in a premixed dump combustor using time-resolved particle image velocimetry". *Combustion and Flame,* ***172***, pp. 309–325. DOI:https://doi.org/10.1016/j.combustflame.2016.06.018.

[41] Aoki, C., Gotoda, H., Yoshida, S., and Tachibana, S., 2020. "Dynamic behavior of intermittent combustion oscillations in a model rocket engine combustor". *Journal of Applied Physics,* ***127***(22), p. 224903. DOI:https://doi.org/10.1063/5.0001900.

[42] Gottwald, G. A., and Melbourne, I., 2004. "A new test for chaos in deterministic systems". *Proceedings of the Royal Society of London. Series A: Mathematical, Physical and Engineering Sciences,* ***460***(2042), pp. 603–611. DOI:https://doi.org/10.1098/rspa.2003.1183.

[43] Armand Eyebe Fouda, J., Bodo, B., Sabat, S. L., and Effa, J. Y., 2014. "A modified 0-1 test for chaos detection in oversampled time series observations". *International Journal of Bifurcation and Chaos,* ***24***(05), p. 1450063. DOI:https://doi.org/10.1142/S0218127414500631.

[44] Toker, D., Sommer, F. T., and D'Esposito, M., 2020. "A simple method for detecting chaos in nature". *Communications biology,* ***3***(1), pp. 1–13. DOI:https://doi.org/10.1038/s42003-019-0715-9.

TABLE 1. Different dynamical states observed by increasing HFF (%) for $P = 10$ kW, 15 kW, and 20 kW for $\phi = 0.65$ and 0.8. The expanded forms of the abbreviations used in the table are provided in the nomenclature section. NA refers to non-availability of data at that conditions due to the breakage of the quartz window allowing optical access to the combustor.

	$\phi = 0.65$			$\phi = 0.8$		
HFF \ P (kW)	10	15	20	10	15	20
0%	CO1	P2	CO1	CO1	P2	P2
10%	I	P2	CO1	CO1	P2	CO2
20%	P1	P2	CO1	CO1	CO2	CO2
30%	P1	P2	P2	CO1	CO2	CO2
40%	P1	P2	P2	I	CO2	CO2
50%	P1	P2	P2	I	P1	CO2
60%	P1	CO2	P2	I	P1	CO2
70%	P1	CO2	I	I	CO2	**NA**
80%	P1	CO2	P1	**NA**	CO2	**NA**

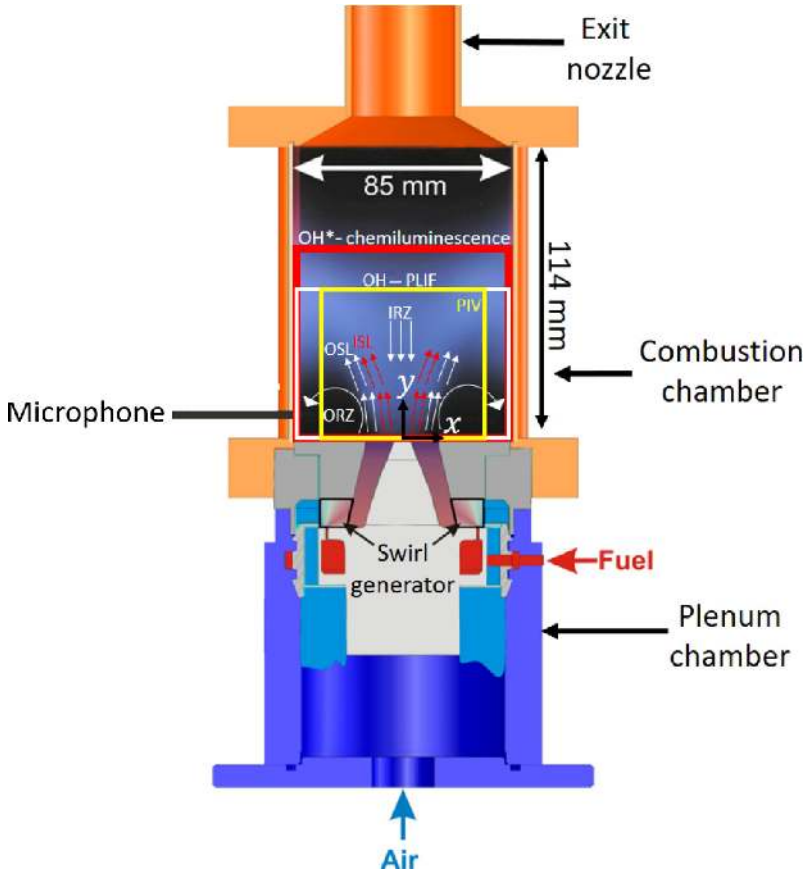

FIGURE 1. Schematic of the experimental setup of the technically premixed gas turbine model combustor.

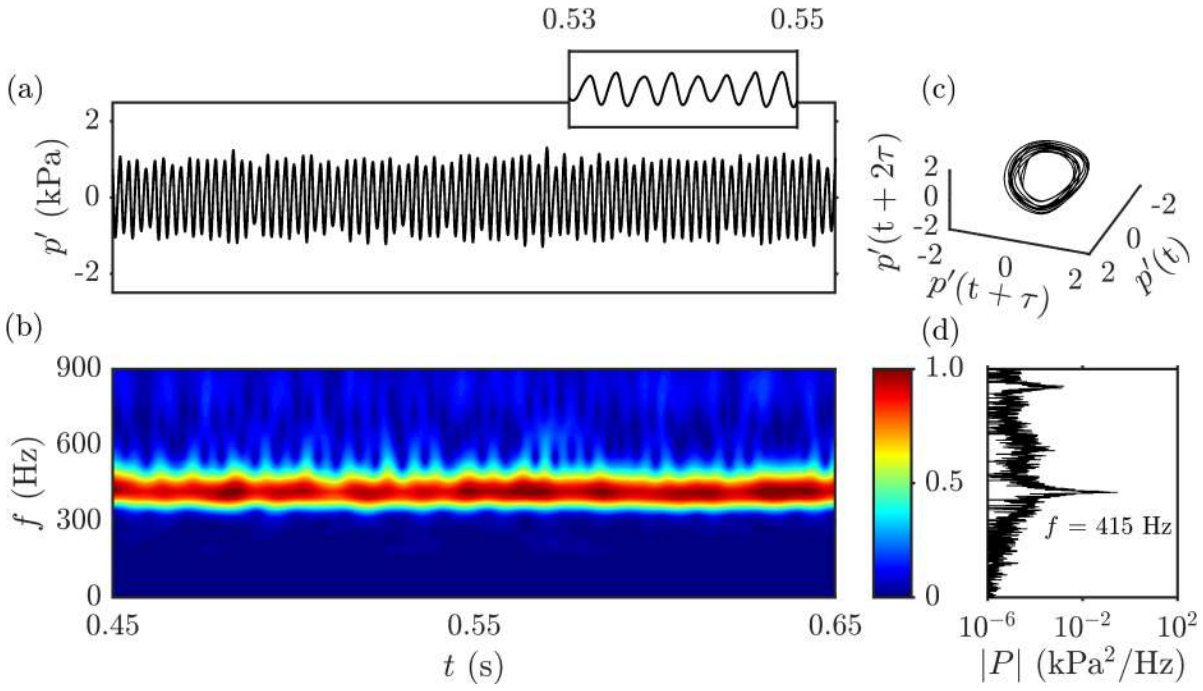

FIGURE 2. (a) The time series (b) scalogram, (c) three-dimensional phase space, and (d) power spectrum of p' during the state of P1 LCO, observed for $P = 20$ kW, $\phi = 0.65$, $HFF = 80\%$, and $Re = 2.29 \times 10^6$.

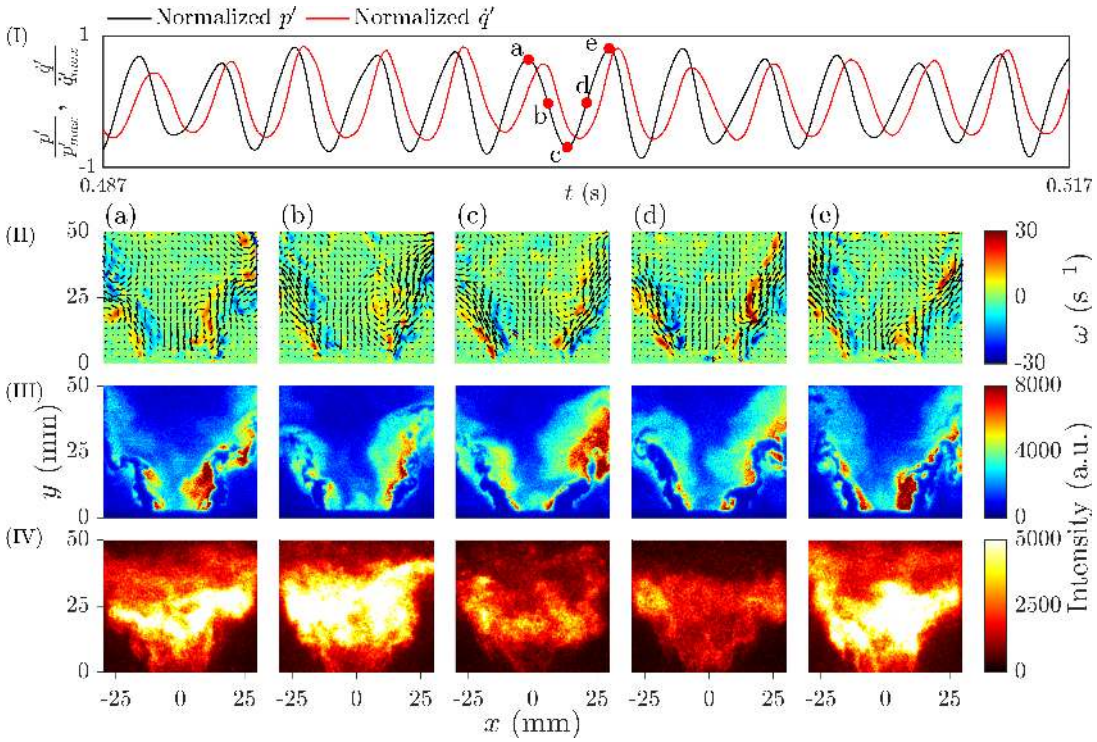

FIGURE 3. (I) The overlapped time series of normalized p' and $\dot{q}'$ fluctuations during the state of P1 LCO. The instantaneous (II) PIV images, (III) OH-PLIF images, and (IV) OH*-chemiluminescence images corresponding to five instants (a-e) over a cycle of p' signal.

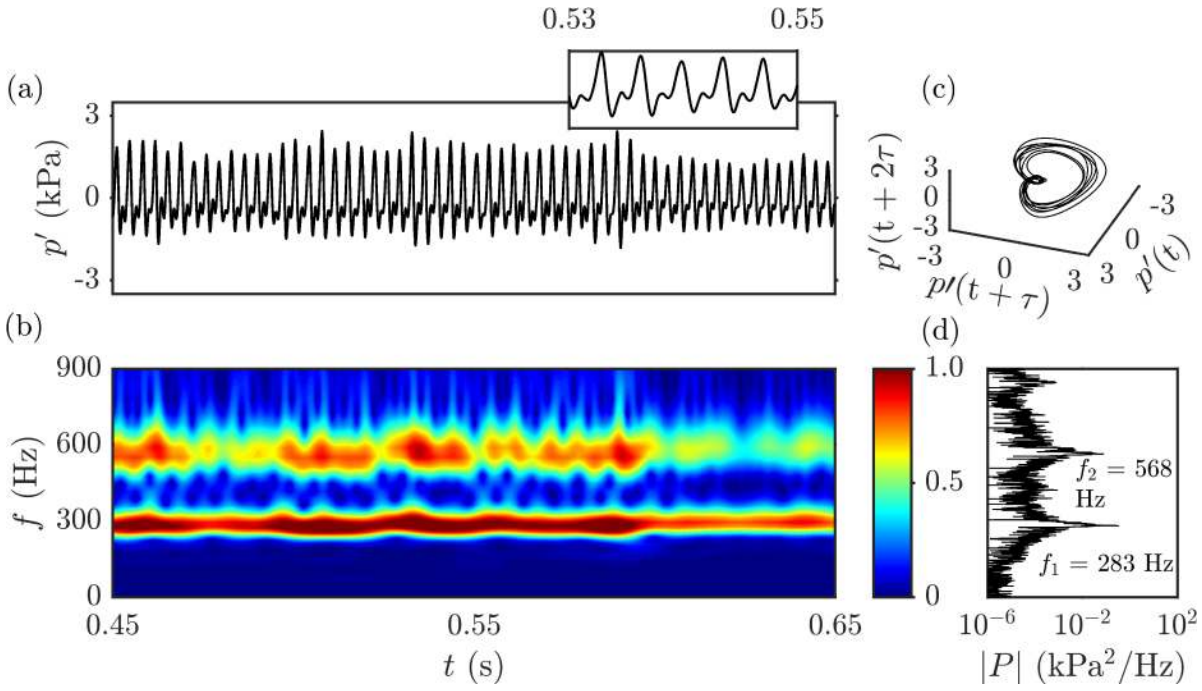

FIGURE 4. (a) The time series, (b) scalogram, (c) three-dimensional phase space, and (d) power spectrum of p' signal during the state of P2 LCO observed for $P = 20$ kW, $\phi = 0.65$, $HFF = 50\%$, and $Re = 2.48 \times 10^6$.

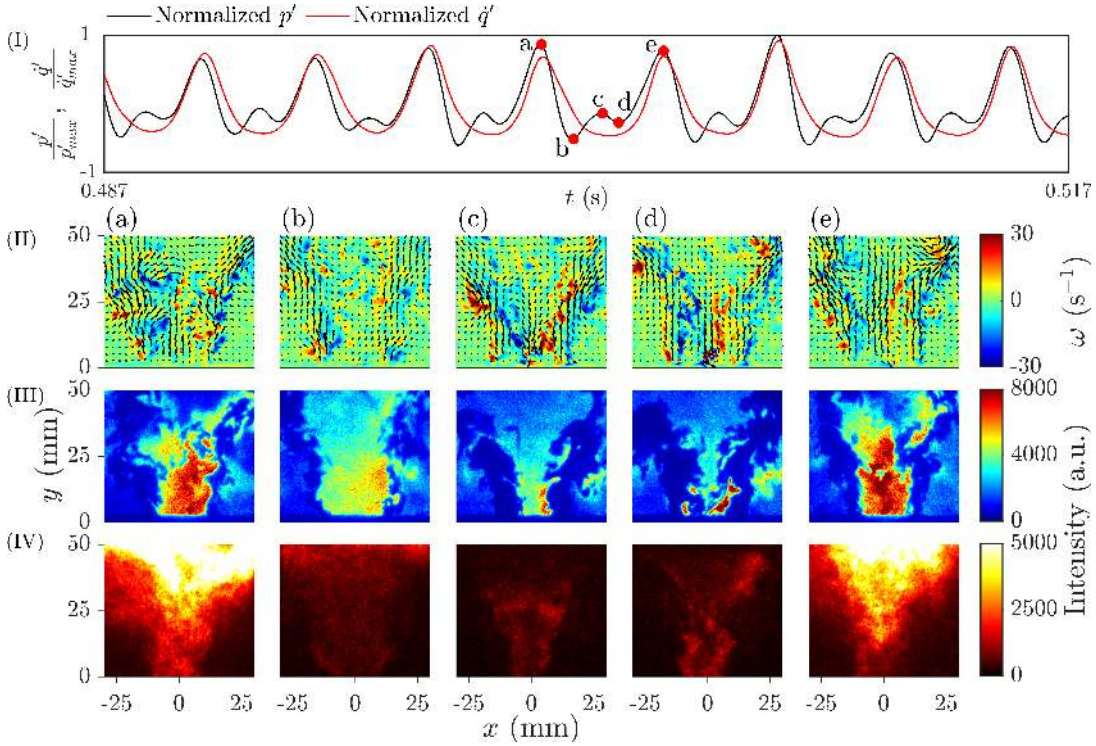

FIGURE 5. (I) The overlapped time series of normalized p' and $\dot{q}'$ fluctuations during the state of P2 LCO. The instantaneous (II) PIV, (III) OH-PLIF, and (IV) OH*-chemiluminescence images corresponding to five instants (a-e) over a cycle of the p' signal.

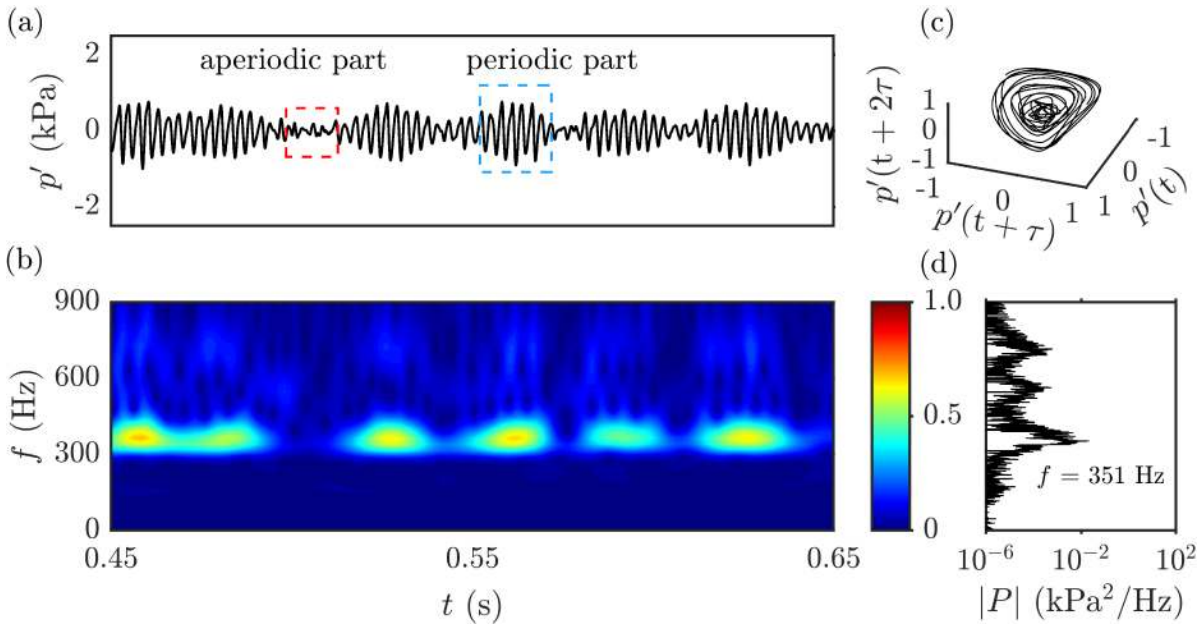

FIGURE 6. (a) The time series, (b) scalogram, (c) three-dimensional phase space, and (d) power spectrum of p' signal during the state of intermittency for P = 20 kW, ϕ = 0.65, HFF = 70%, and Re = 2.38 × 10^6.

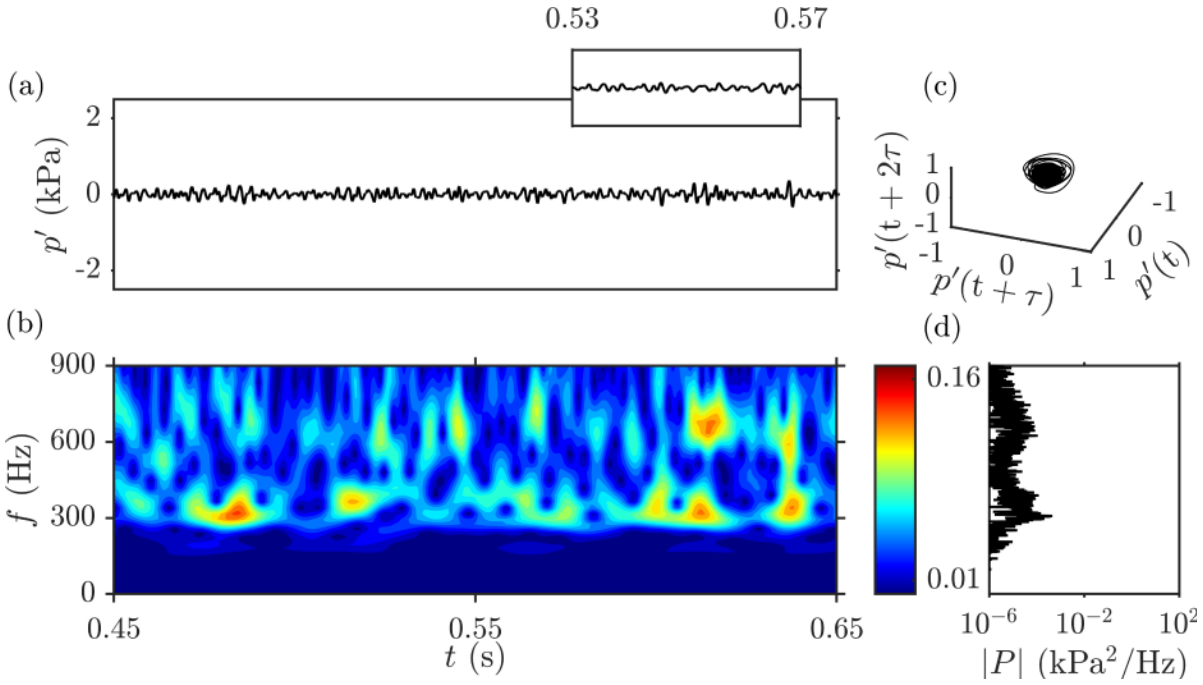

FIGURE 7. (a) The time series, (b) scalogram, (c) three-dimensional phase space, and (d) power spectrum of p' during chaotic state-1 (CO1), observed for P = 20 kW, ϕ = 0.65, HFF = 0%, and Re = 2.61 × 10^6.

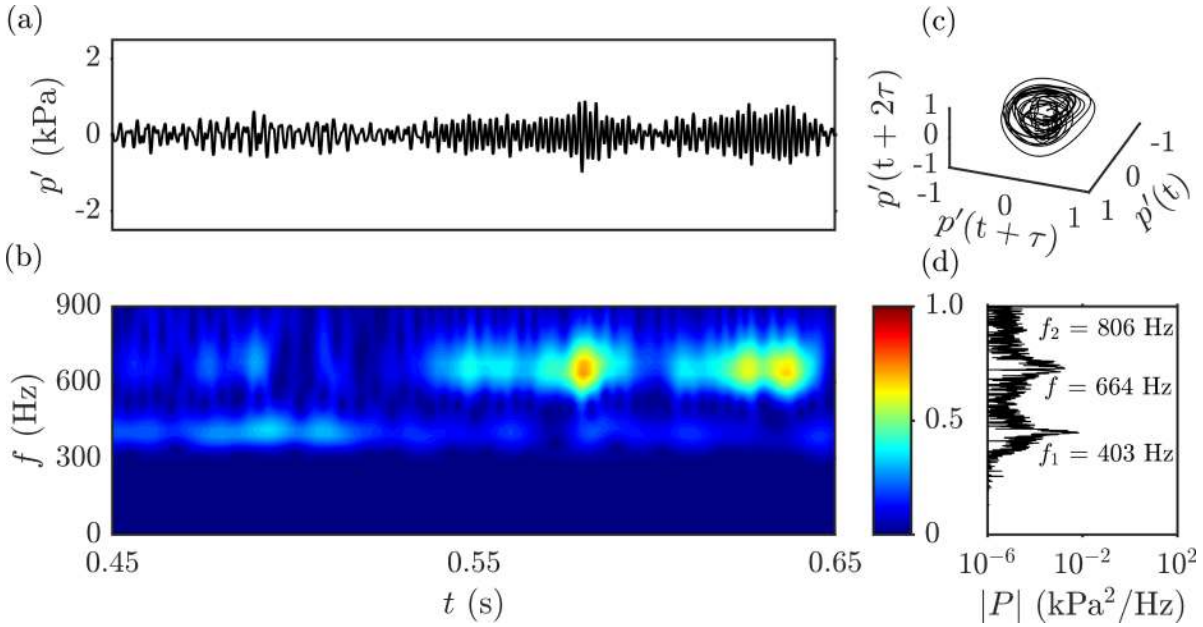

FIGURE 8. (a) The time series, (b) scalogram, (c) three-dimensional phase space, and (d) power spectrum of p' signal during chaotic state-2 (CO2) for $P = 15$ kW, $\phi = 0.8$, $HFF = 70\%$, and $Re = 1.48 \times 10^6$.

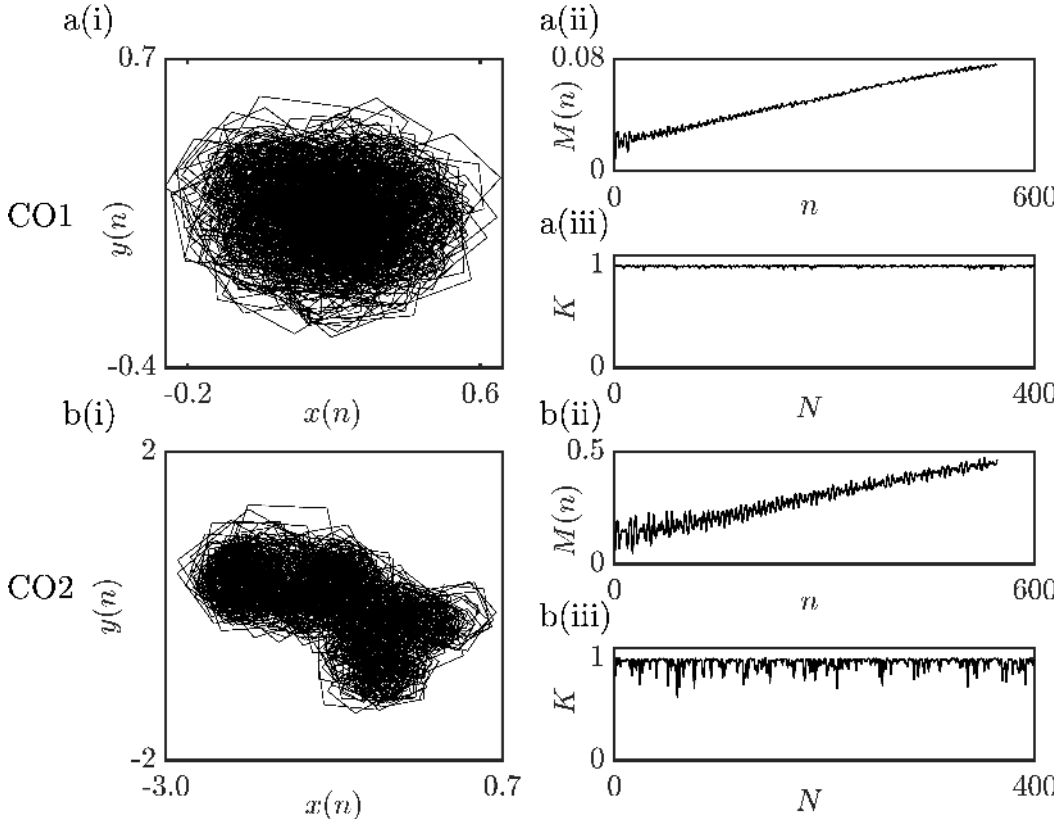

FIGURE 9. 0-1 test performed for chaotic state-1 (Fig. 7a) and chaotic state-2 (Fig. 8a). (i) The plot between the translation variables $x(n)$ and $y(n)$, (ii) the behaviour of mean square displacement $M(n)$ with n, and (iii) the variation of the growth rate K with N.

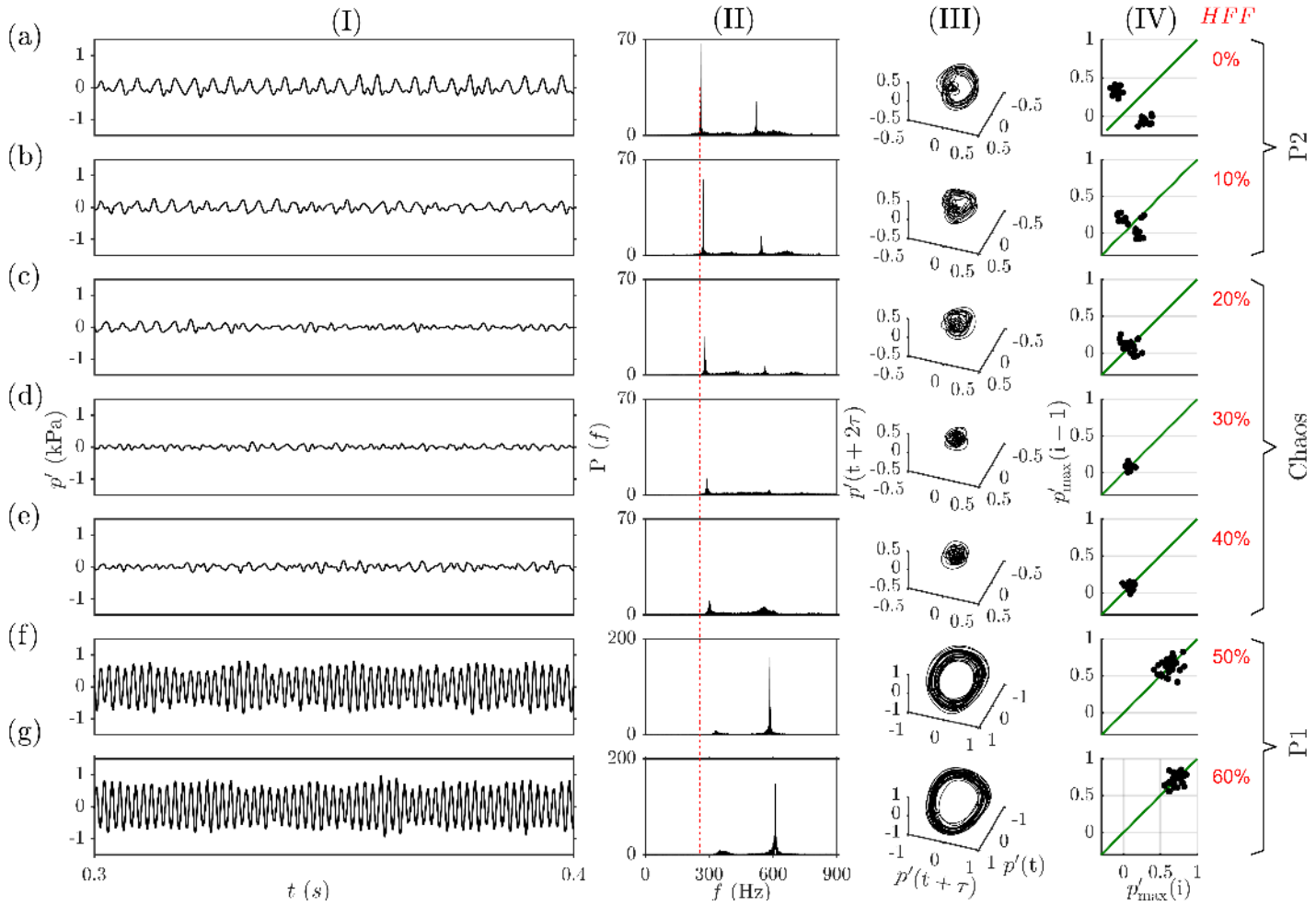

FIGURE 10. The effect of increasing HFF in the fuel on the acoustic oscillations is presented using (I) time series, (II) amplitude spectrum, and (III) three-dimensional phase space, and (IV) first return map of p' oscillations. Only the HFF is varied from 0% to 60% in steps of 10% while maintaining $P = 15$ kW and $\phi = 0.8$. A red colored dotted line in (II) represents the frequency of the fundamental mode in the combustor for 0% HFF.

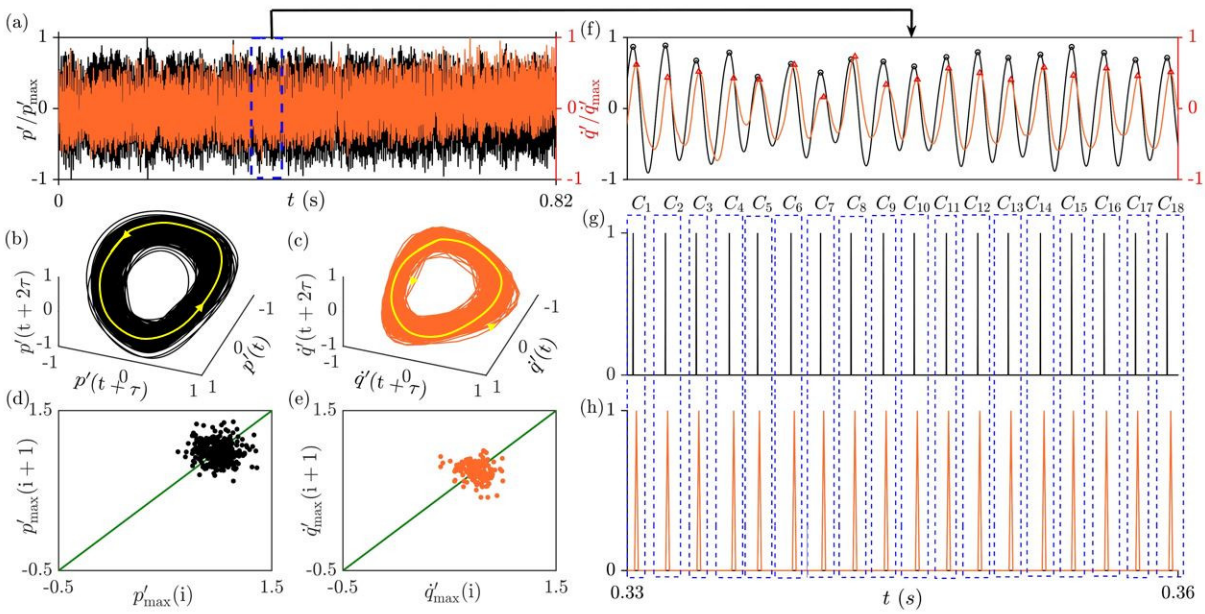

FIGURE 11. Illustration of 1:1 frequency locking between p' and $\dot{q}'$ signals during the state of period-1 LCO. (a) Time series of the normalized p' (black line) and $\dot{q}'$ (orange line) signals, (b, c) the corresponding phase spaces, and (d, e) first return maps for $P = 15$ kW, $\phi = 0.8$ and $HFF = 50\%$. (f) The zoomed view of the signals with markers corresponding to the local maximas. (g, h) The spiking signals indicating the locations of local maxima in p' and $\dot{q}'$ oscillations, respectively. $C_1, C_2, \ldots$ in (g) represent the number of cycles, and blue dotted boxes contain the number of peaks in one oscillation cycle of p' and $\dot{q}'$ signals.

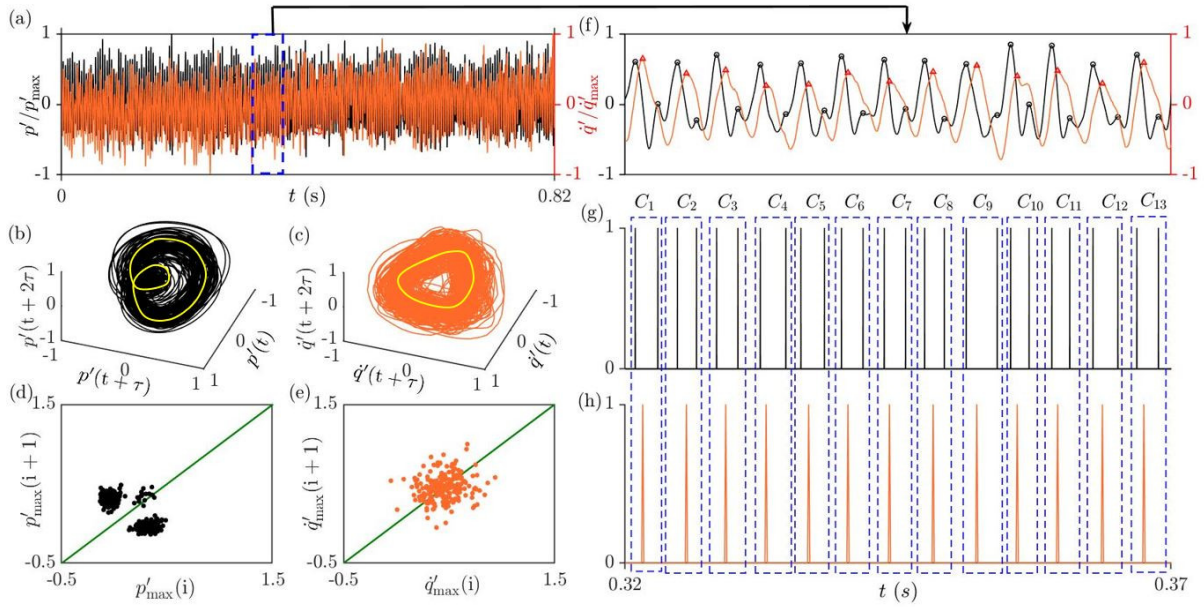

FIGURE 12. Depiction of 2:1 frequency locking between p' and $\dot{q}'$ signals during the state of P2 LCO. (a) Time series of normalized p' (black line) and $\dot{q}'$ (orange line) signals, (b, c) the corresponding phase spaces, and (d, e) first return maps for the conditions of $P = 15$ kW, $\phi = 0.8$ and $HFF = 0\%$. The description of (f, g, h) is the same as that in Fig. 11.

Supplementary material

S1. Calculation of adiabatic flame temperature

We calculated the adiabatic flame temperature for all operating conditions investigated with increasing hydrogen fuel fraction (HFF) using the GASEQ software. As we notice from Fig. S1, with an increase in HFF for a particular thermal power (P = 15 kW) and equivalence ratio (ϕ = 0.8), the adiabatic temperature of the flame continuously increases by about 100 K. As a result, the speed of sound also increases with the hydrogen-enrichment, leading to shift in the frequency of dominant modes of thermoacoustic oscillations to a higher value.

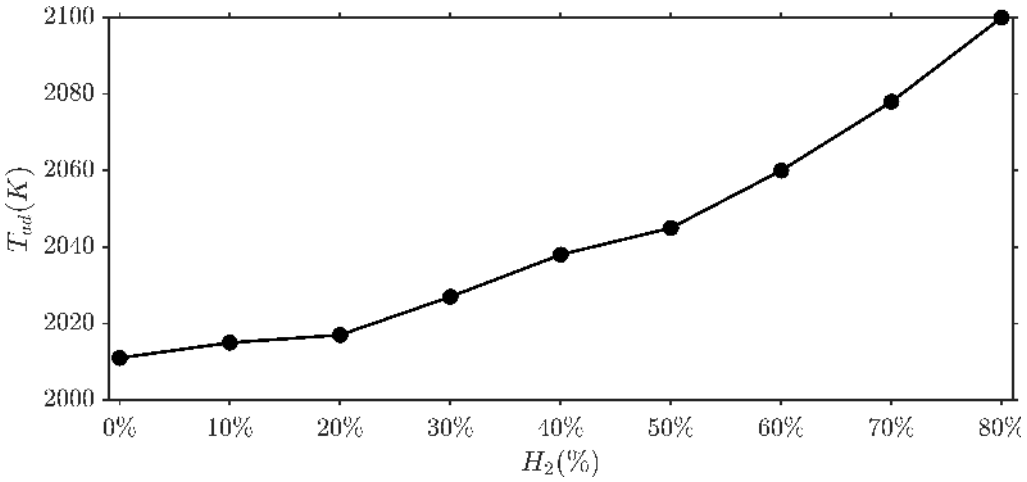

FIGURE S1: Adiabatic flame temperature (in K) with increase HFF for the operating condition P = 15 kW and ϕ = 0.8.

S2. Coupled analysis of Acoustics, flame and flow dynamics

1. Intermittency

In this section, we briefly present the behavior of the flame and flow interacting with the acoustic field during the state of intermittency. Figure S2 show the normalized p' and $\dot{q}'$ signals (Fig. S2-I), instantaneous vorticity fields obtained from PIV (Figs. S2-II), the heat release rate region of the flame measured over the central plane using from OH-PLIF (Figs. S2-III), and the line-of-sight integrated heat release rate measurements obtained from the OH*- chemiluminescence images (Figs. S2-IV). These images correspond to five time instants (a - e) marked on the p' signal in Fig. S2-I during the epoch of low amplitude aperiodic oscillations of the intermittency state that exhibits a switching between epochs of aperiodic and periodic oscillations. From Fig. S2-II, we observe that the asymmetric generation of small-scale vortices continuously along the inner shear layer (ISL) and outer shear layer (OSL) of both the left and right branches of the flame. We also notice that the flame is always stabilized between the inner shear layer and the outer shear layer along the two branches (Figs. S2-IIIa-e). We observe a moderate wrinkling on the flame front due to the swirling in the flow. We do not observe significant variations of the flame size and length during the aperiodic epoch of oscillations (Figs. S2-III). From the corresponding OH*-

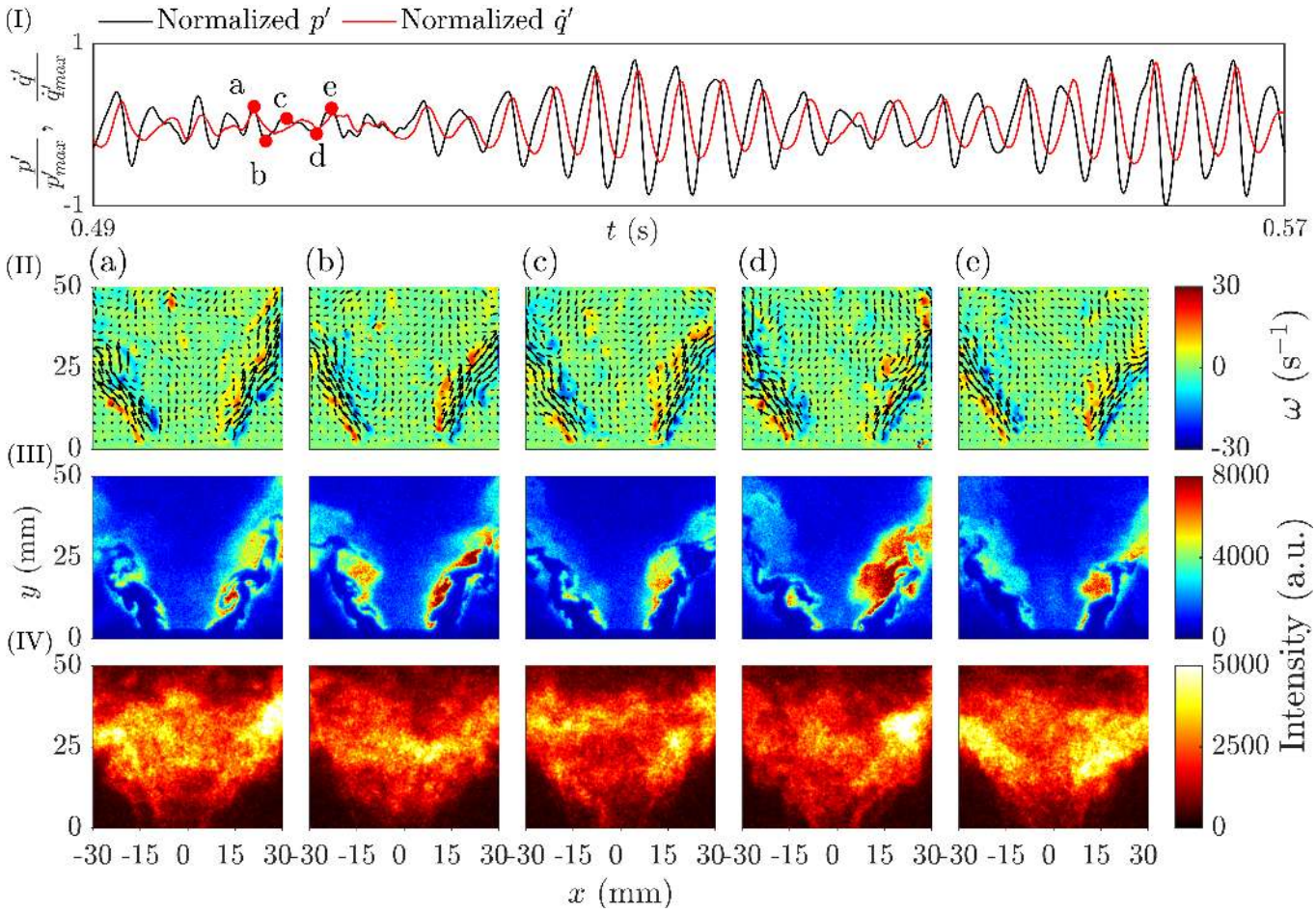

FIGURE S2: The time series of normalized p' and $\dot{q}'$ fluctuations during the aperiodic epoch in the state of intermittency. The corresponding (II) PIV (III) OH-PLIF, and (IV) OH*- chemiluminescence images.

chemiluminescence images of the flame (Figs. S2-IVa-e), we notice that the flame behavior is similar across different time instances as we do not see any significant change in the shape of the flame. However, at the instances of high positive amplitude oscillations (Figs. S2-IVa,e), we observe a small increase in the flame intensity at some spatial locations.

We observe that there is a phase difference between normalized p' and $\dot{q}'$ during the P1 oscillations in intermittent state switching between aperiodic and periodic oscillations (Fig. S3-I). Here, we notice higher vorticities compared to the flow field during the aperiodic region (Figs. S3-IIa-e). We observe significant intensity variations in the flame stabilized in the region between the ISL and OSL along both the branches (Figs. S3-IIIa-e) with the variation of the pressure from its maxima to minima and so on. When the pressure amplitude is near to its maxima (Fig. S3-Ia), we observe the asymmetric emergence of vortices in ISLs (Figs. S3-IIa,d and e) and very high flame intensity (Figs. S3-IIIa,e). The flame shape widens from maxima to minima of p'. As the pressure reaches its minima (Fig. S3-Ic), the thickness of OSL increases while the inner recirculation zone (IRZ) remains unchanged (Fig. S3-IIIc). Due to phase shift, we observe the minimum flame intensity (Fig. S3-IIId) at instant d, which is very near to minima of the heat release rate (Fig. S3-IVd).

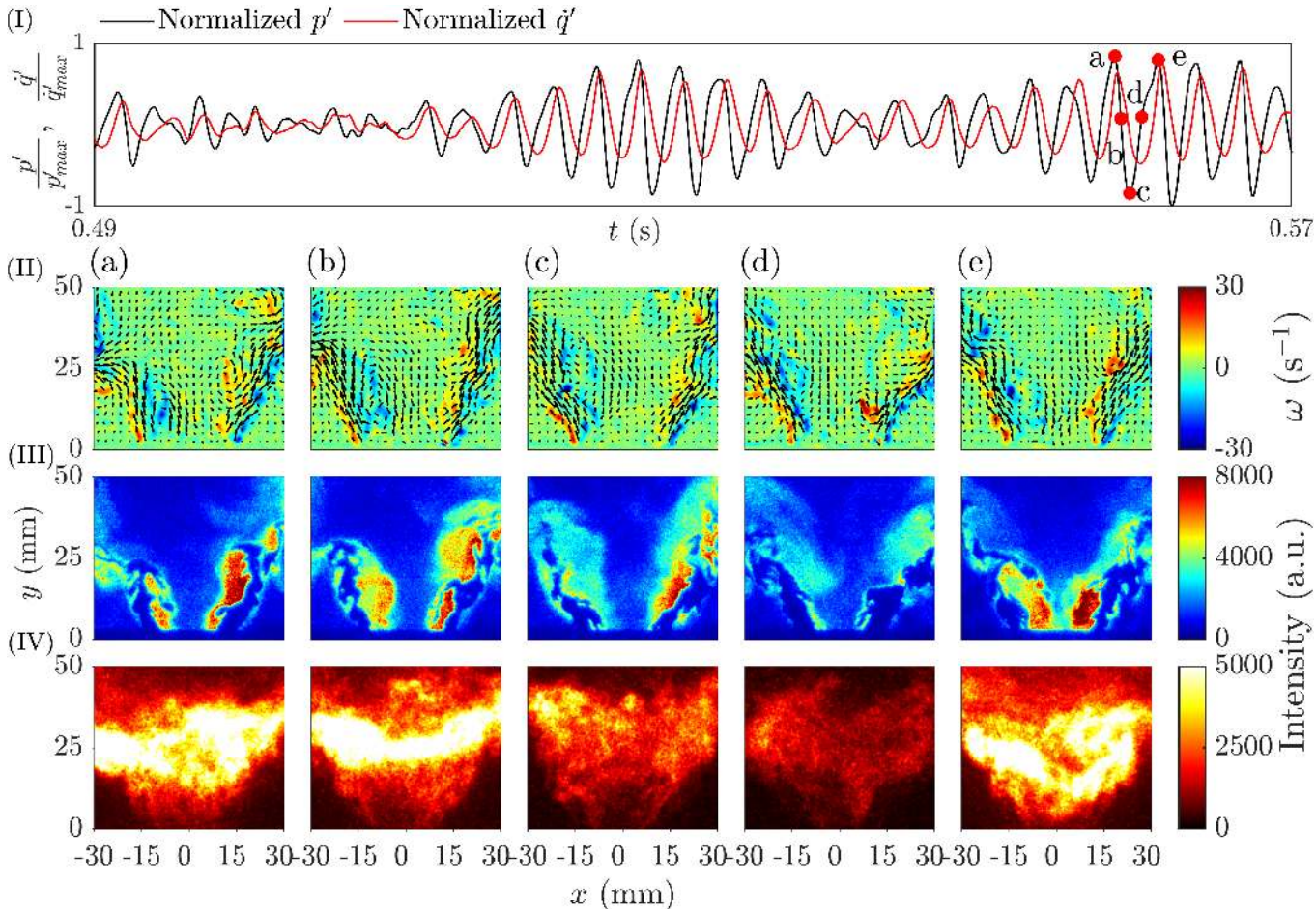

FIGURE S3: (I) The time series of normalized p' and $\dot{q}'$ fluctuations for five instants (a-e) during one periodic cycle in the state of intermittency. The corresponding (II) PIV (III) OH-PLIF, and (IV) OH*- chemiluminescence images.

2. Chaotic oscillations

This section represents the dynamics of the flame and flow during chaotic state-1 and chaotic state-2.

Figure. S4 shows the normalized p' and $\dot{q}'$ signals (Fig. S4-I), instantaneous images of the flow and vorticity fields obtained from PIV (Fig. S4-II), the distribution of OH molecules over the central plane using OH-PLIF (Fig. S4-III), and the line of sight integrated OH*-chemiluminescence field (a measure of heat release rate distribution) during chaotic state-1 (CO1) in the system (Fig. S4-IV). These images correspond to five time instants (a)-(e) marked on the p' signal (Fig. S4-I). Only the common regions covered by all the three imaging techniques are shown. From Fig. S4II, we observe that several small-scale vortices are generated irregularly along the inner and outer shear layers in both the left and right flame branches. We also notice that the V-shaped flame is always stabilized in the region between the inner shear layer (ISL) and outer shear layer (OSL) along the two branches (Fig. S4-III). We observe moderate wrinkling of the flame front due to the swirling action in the flow. We do not observe significant changes in the flame size and length over time (Fig. S4-III). From the corresponding OH*-chemiluminescence images of the flame (Fig. S4-IV), we observe that the flame

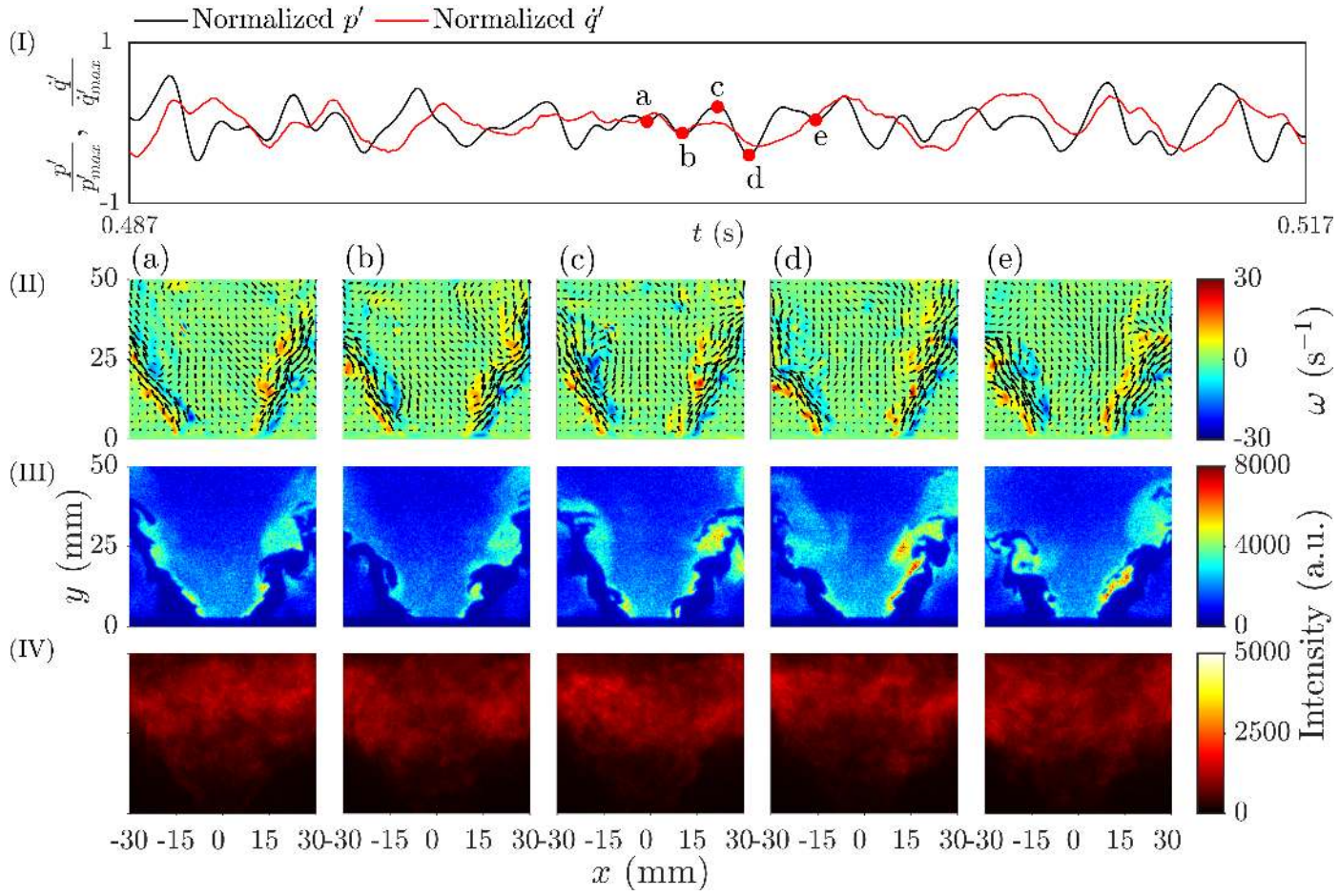

FIGURE S4: (I) The time series of normalized p' and $\dot{q}'$ fluctuations for five instants (a-h) during different instants indicating the local maxima and minima in chaotic state-1. The corresponding (II) PIV (III) OH-PLIF, and (IV) OH*- chemiluminescence images.

behavior is similar across different time instances as we do not see any much change in the flame intensity.

The flame stabilizes in both IRZ and ORZ along two separate branches of the flame front (Figs. S5-IIIa-h) for any time instant during the state of chaotic state-2 (CO2). When the pressure is at its first maxima (Fig. S5-Ia), we do not observe any vortex with significant vorticity level (Fig. S5-IIa). The corresponding flame image (Fig. S5-IIIa) shows a moderate intensity. The chemiluminescence image at this instant (Fig. S5-IVa) shows that the flame is compact and the distribution of the heat release rate is concentrated at a small distance from the dump plane. As the pressure reaches its first minima (Fig. S5-Ib), the vorticity (Fig. S5-IIb) and the flame intensity in the IRZ do not change significantly (Fig. S5-IIIc). The corresponding chemiluminescence image (Fig. S5-IVb) indicates a reduction in the heat release rate distribution. On proceeding to the second maxima (Fig. S5-Ic) and second minima (Fig. S5-Id) on the p' signal, the vortices with symmetric behavior are observed (Figs. S5-IIIc,d) and the flame gradually widens (Figs. S5-IVc,d). The heat release rate distribution becomes compact and is shifted to near the dump plane (Fig. S5-IVc) and again shifted to slight away (Fig. S5-IVd) from the dump plane. After the pressure crosses its second minima, we observe that the vortices initially shed at the second maxima, convects

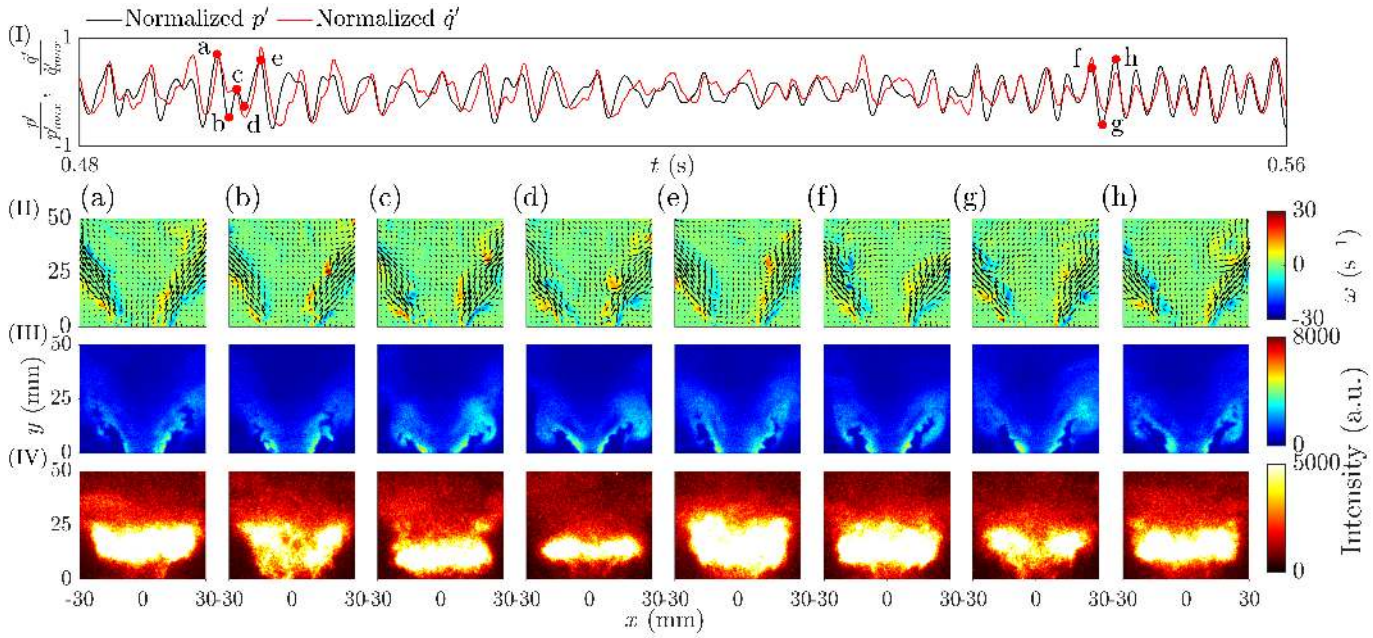

FIGURE S5: (I) The time series of normalized p' and $\dot{q}'$ fluctuations for five instants (a-h) during different instants indicating the local maxima and minima in chaotic state-2. The corresponding (II) PIV (III) OH-PLIF, and (IV) OH*- chemiluminescence images.

outside the window

During another instants (f-h) in chaotic state-2, we observe that p' and $\dot{q}'$ are almost phase-locked (Fig. S5-I). Here, we see vortices with low vorticity in the flow field (Figs. S5-IIa-e). we observe moderate intensity in the flame stabilized in the region between the ISL and OSL along both the branches (Figs. S5-IIIf-h) with pressure variation. The corresponding chemiluminescence images show compact behavior of the heat release rate distribution near the dump plane (Figs. S5-IVf,h). When the pressure amplitude is at its maxima (Fig. S5-If), we notice the asymmetric emergence of vortices in ISLs and moderate flame intensity in the flow field (Figs. S5-IIIf,h). The flame shape is not changing significantly with change in pressure. As the pressure nears its minima (Fig. S5-Ig), again a pair of votices is observed to be shed. The heat distribution appears to be divided into two regions (Fig. S5-IVg). As pressure again increases, we see the regions of the heat release rate distribution unite (Fig. S5-IVh).

Overall, we observe dramatic changes in the flame and flow dynamics during chaotic state-2, which is completely different from the state of thermoacoustic instability with period-1 and period-2 oscillations (please refer to the manuscript Figs. 3 and 5) and intermittency (Figs. S2 and S3).

S3. 0-1 test analysis and Chaos Decision Tree algorithm -

The output of the 0-1 test is highly dependent on the sampling of the signal (Fouda *et al.* 2014, Melosik *et al.* 2016). Therefore, we undersampled the original signal (sampled at 100 kHz) to various levels (20 kHz, 10 kHz, 6.67 kHz, 5 kHz, 4 kHz, 3.33 kHz, 2.85 kHz and 2.5 kHz). We then tested the consistency of the chaos test using a periodic signal at the aforementioned undersampling levels

(Marszalek *et al.* 2019). We found that the undersampled signal having sampling rate 6.67 kHz to be consistent. Higher undersampling beyond this sampling rate leads to the destruction of key features (e.g., locations of maxima, minima, amplitude) in the oscillations of the pressure signal. Hence, we have undersampled the original signal from a sampling rate of 100 kHz to 6.67 kHz for chaotic state-1 (Fig. 7 in the manuscript) and chaotic state-2 (Fig. 8 in the manuscript). This corresponds to 22 and 19 points per cycle for chaotic state-1 and chaotic state-2, respectively

We also confirmed our results with the recently developed novel algorithm for chaos test by Toker *et al.* (2020), called Chaos Decision Tree algorithm. The key steps of this algorithm are as follows: The first step is the calculation of permutation entropy (a quantification measure of the complexity of a dynamic system by capturing the order relations between time series and extracting a probability distribution of the ordinal patterns) of data and check whether the signal is stochastic or not (Zunino *et al.* 2017). If the signal is not stochastic, the next step includes de-noising the signal using the Schreiber algorithm (Schreiber *et al.* 1993). Then, we perform a test to check the effect of oversampling of the signal using the difference between the global maxima and minima. If this difference is greater than 10 times of the mean absolute difference between consecutive values in the signal, then the data will be undersampled by skipping every alternate point in the provided signal for test. Again, the same check is performed for oversampling, until the data is sampled correctly. Then, the 0-1 test is used to decide the existence of chaos in the signal.

The advantage of the Chaos Decision Tree algorithm is that it automatically takes care of oversampling effects of the signal. It also classifies the property of the signal as stochastic, periodic, or chaotic oscillations. We have used the MATLAB code provided in Toker *et al.* (2020). The output of this code provides the information of the property of a time series as periodic, stochastic or chaotic. It also provides the value of the median of K of the modified 0-1 test. We are providing the results obtained for the data presented in Figs. 7 and 8 (in the manuscript).

In conclusion, chaotic state-1 and chaotic state-2 (as defined in the manuscript) exhibits chaos, which has been verified with the help of 0-1 test for chaos and confirmed with the help of Chaos decision Tree algorithm.

S4. Weakly periodic limit cycle oscillations –

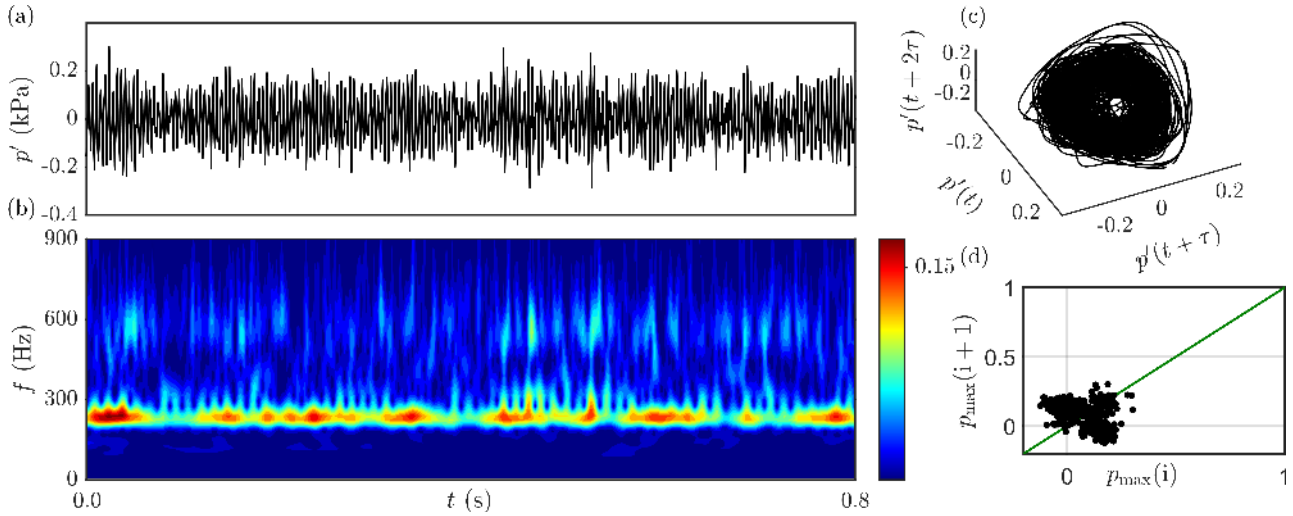

FIGURE S6: (a) The time series, (b) scalogram, (c) three-dimensional phase space, and (d) power spectrum of p' signal during the state of P2 LCO observed for P = 10 kW, ϕ = 0.65, HFF = 20%, and $Re = 1.3 \times 10^6$.

For P = 10 kW and ϕ = 0.65, we observe weakly periodic limit cycle oscillations for HFF = 20% and 30%. Since the amplitude of the limit cycle oscillations are low, turbulent fluctuations can significantly influence the amplitude envelope of the p' signal. As a result, in the scalogram, even though we observe a consistent band of frequency around 232 Hz, its amplitude varies in time. Due to the strong influence of turbulent fluctuations, the ring structure in the phase space is not apparently identified. Similarly, the return map shows a clutter of points near the lower end of the diagonal line.